Lower crustal magmatic processes and andesite genesis at Shiveluch Volcano

Andrea E. Goltz*[1,2] and Michael J. Krawczynski[2]
[1] Carnegie Institution for Science, Earth and Planets Laboratory
[2] Washington University in St. Louis, Department of Earth, Environmental, and Planetary Science
* agoltz@carnegiescience.edu [corresponding author]
ORCiD (AEG): 0000.0002.7282.1604
ORCiD (MJK): 0009.0007.0254.4000
Keywords: arc volcanism; subduction zone; crystallization; experimental petrology; crustal melting; hydrous magma

This manuscript has been submitted for publication in Volcanica. Please note that this manuscript is currently under revision after peer-review, and subsequent versions of this manuscript will have slightly different content. If accepted, the final version of this manuscript will be available via Peer-reviewed Publication DOI on this webpage.

Abstract

The silicic melts that eventually erupt at arc volcanoes are produced in the lower crust, yet, the storage conditions of magma in the lower crust have not been the topic of extensive study. In this study, we conduct and analyze hydrous piston cylinder experiments to determine the mid-to-lower magma storage conditions of primitive melt at Shiveluch, an arc volcano located in northern Kamchatka. The near-liquidus assemblage of amphibole and olivine, observed in mafic enclaves, constrains storage of primitive magmas to pressures between 500 MPa and 1 GPa, temperatures from 1000-1100 °C, and high (≥7.2 wt%) H_2O contents. Compositions of glasses in our experiments also show that lower crustal differentiation cannot be the only process involved in the production of andesites at Shiveluch. By comparing synthetic and natural compositions of amphibole we determine that anatexis of the lower crust is also likely to significantly contribute to produce andesitic melts at Shiveluch.

Introduction

The lower crust sets the stage for upper crustal magmatic processes and eruptions at arc volcanoes. Continued addition of hot, primitive magma from the mantle to the bottom-most crust establishes a lower crustal "hot zone" where magmas evolve (e.g., Annen et al., 2006). Fractional crystallization of olivine, pyroxenes, and amphibole from primitive magmas in the lower crust can produce the relatively silicic melts that are stored and partially crystallized in the upper crust (e.g., Sisson et al., 2005; Blatter et al., 2013; Nandedkar et al., 2014; Blatter et al., 2017; Ulmer et al., 2018). Melting of surrounding lower crustal rocks can also produce intermediate to silicic melts with more energetic efficiency than fractional crystallization (e.g., Blatter et al., 2017; Till et al., 2019; Blatter et al., 2023). Some combination of both processes produces the silicic magmas that erupt at arc volcanoes.

Despite the importance of the lower crust to the trans-crustal magma system, pressures and temperatures of magma storage are more commonly estimated for silicic magmas in the upper crust. Storage conditions provide quantitative constraints on conceptual models of crustal structure. They can be directly compared to the depths of earthquakes to relate chemical processes to earthquakes (e.g., Dayton et al., 2023) or compared to other geophysical constraints on the current depths of magma storage (as done in Wieser et al., 2023). Storage conditions of magmas in the upper crust have been assessed by application of rhyolite-MELTS (e.g., Gualda et al., 2012; Pamukcu et al., 2015; Harmon et al., 2024) or empirically calibrated mineral and melt thermobarometers (e.g., Putirka, 2008; Wieser et

al., 2022), analysis of volatiles in melt inclusions (e.g., Barth et al., 2024), and experimental determination of phase diagrams (e.g., Hammer et al., 2002; Rutherford and Devine, 1996). Because amphibole may crystallize from hydrous melts in the lower crust, some of these methods cannot be used to estimate lower crustal magma storage conditions. For example, rhyolite-MELTS cannot predict amphibole stability, which inhibits its use in this scenario. Additionally, the signatures of lower crustal processes can be difficult to isolate from the signatures of upper crustal processes in erupted silicic magmas. These challenges limit the assessment of lower crustal magma storage conditions.

In this study, we take an experimental approach to determine the mid-to-lower magma storage conditions of primitive melt at Shiveluch, an arc volcano located in northern Kamchatka. Shiveluch has had more VEI 4+ eruptions in the Holocene than any other volcano (Global Volcanism Program, Smithsonian Institution), and thus it is particularly consequential to understand the magmatic processes occurring beneath it. The compositions of a basalt and basaltic andesite hypothesized to reflect the compositions of magmas feeding the Shiveluch crustal plumbing system are preserved in two tephra units (Volynets et al., 1997; Ponomareva et al., 2007). In their study of mafic enclaves, Goltz et al. (2020) identified a likely near-liquidus phase assemblage of amphibole, olivine, and clinopyroxene. Using mineral thermometry and hygrometry, they showed that magmas with water contents of at least 10 wt% were stored in the lower crust at ~1060°C and at a minimum of 16 km depth. Here, we experimentally constrain the phase relations of the two hypothesized primitive magma compositions at a range of water contents and temperatures at mid-to-lower crustal pressures (500 MPa and 1 GPa). The resulting phase diagrams are used to isolate pressures, temperatures, and water contents at which the near-liquidus assemblage of amphibole, olivine, and clinopyroxene is stable and, thus, determine the likely pressures, temperatures, and water contents of primitive magmatic storage. Additionally, using the chemistry of synthetic glass and amphibole, we constrain the processes involved in producing intermediate magmas at Shiveluch.

Methods

Starting material synthesis and capsule Fe-saturation

Equilibrium crystallization experiments were conducted on starting compositions representative of the major element composition of tephra erupted at Shiveluch 3959 BP and 8363 BP or related to these compositions by fractional crystallization or olivine addition (**Table 1**). The 3959 BP tephra major element composition is more

magnesian and potassic than the 8363 tephra and both have been proposed as representing potential parental composition of magmas at Shiveluch (e.g., Volynets et al., 1997; Goltz et al., 2020); throughout this study, the 3959 BP tephra starting composition will be referred to as "hi-K" and the 8363 BP tephra composition will be referred to as "lo-K". By conducting experiments on the tephra compositions and their evolved derivatives, we seek to partially simulate the effects of equilibrium and fractional crystallization on phase equilibria and chemistry.

Experiments were run water saturated, water undersaturated with no added CO_2, or water undersaturated with mixed volatiles (i.e., H_2O and CO_2). Non-mixed volatile experiments were prepared by dehydrating and decarbonating starting mixes and adding free water to the starting mix during capsule preparation, whereas mixed volatile experiments were conducted on mixes with added gibbsite and carbonates. In total, eight synthetic mixes were used in this study, and their compositions (confirmed by and with uncertainties based on repeated electron probe microanalysis of glassed mixes) are reported in **Table 1**.

To prevent excessive iron loss, gold capsules were used in experiments run in experiments at or below 1100°C. For higher temperature experiments, Fe-saturated gold-palladium (80:20) capsules were used. The capsules were saturated using a method after Blatter et al. (2013). To saturate the $Au_{80}Pd_{20}$ capsules, the capsules were packed with and surrounded by a 2:1 mixture by weight of magnetite and clear jewelry enamel in a large Pt crucible. The packed crucible was suspended in a gas mixing furnace at 1100°C with a flow of CO_2-H_2 gas to control the f_{O2} at NNO for about a week, after which the crucible and capsules were cleaned by immersion and sonication in hydrofluoric acid for 2-4 days. Success of the Fe-saturation procedure was confirmed by measurement of Fe in two saturated capsules using EPMA. We analyzed 34 line-scans using a traditional background correction method (rather than the mean atomic number correction used for our analyses of silicates) across the two capsules and found that the alloy was $Au_{78}Pd_{19}Fe_3$ throughout, approximately consistent with values calculated using the equations and procedure of Balta et al. (2011). For these analyses, we used the nominally iron-free $Au_{80}Pd_{20}$ tubing used to form the capsules before iron saturation as a primary standard for gold and palladium and a National Bureau of Standards (NIST) stainless steel standard (NBS160a) as the primary standard for iron. Success of the Fe-saturation of $Au_{80}Pd_{20}$ capsules was also evaluated using a mass balance calculation of Fe-loss for all experiments. The maximum Fe-loss observed in successful experiments was ~21%, but the average Fe-loss in the AuPd capsules was much more moderate in general, averaging 9% (**Table 2**).

Experimental Procedures

Capsule Design

Experiments used a nested capsule design. A Pt buffer capsule packed with 20-30mg of a 5:1 molar mixture of Ni:NiO and an Au or $Au_{80}Pd_{20}$ sample capsule packed with 30mg of the starting mix were surrounded with and separated by Al_2O_3 powder in a larger diameter gold or gold palladium outer capsule. For water saturated and water undersaturated experiments with no mixed volatiles, free water was added to all capsules (2 or 3 μL in the Pt buffer capsule, 3 or 6 μL in the sample capsule, and 10 or 20 μL in the outer capsule). For mixed volatile experiments, 1 μL of free water was only added to the Pt buffer capsule and outer capsule to mitigate water loss through diffusion and to equilibrate oxygen fugacity in the experiment with the buffer. After packing, all capsules were crimped straight across (Pt buffer capsule) or in a three-fin design (sample and outer capsules) and welded shut using a tungsten-inert gas micro-arc welding. Leaks were checked for by weighing, heating in a 149°C oven for 2 minutes, and reweighing the capsule three times. After showing no leaks, the outer capsule was compressed to a final height of 7-8.5 mm.

Piston Cylinder

Experiments were conducted using piston cylinder apparatuses at Washington University in St. Louis at either 1 GPa or 500 MPa using a 12.7 mm or 19.1 mm pressure vessel bore diameter, respectively, and details of the assembly are described in Goltz et al. (2022). Experimental temperature ranged from 900 to 1205°C and experimental duration ranged from 12 to 52 hours (**Table 2**).

Experiments at 1 GPa were conducted using a barium carbonate pressure medium. The experiments were first pressurized to 1 GPa and then heated at 50°C/min to the target temperature, with a 6-minute dwell in the temperature ramp at 865°C. 0.5 GPa experiments were run using an assembly with a pyrex or fused silica glass sleeve separating the graphite furnace from the NaCl pressure medium. Pyrex sleeves were used for experiments at temperatures ≤1125°C, and fused silica glass sleeves were used at higher experimental temperatures. For all but two experiments (F174 and F175), samples were pressurized and then heated at 15°C/min to the target temperature with a 24-minute dwell at 600°C. F174 and F175 were pressurized and then heated at 50°C/min to the target temperature with a 6-minute dwell at 600°C.

Experimental Charge Evaluation

In all cases, experimental success was initially evaluated upon inspection of the quenched experimental charge. The outer capsule was punctured with a small drill-bit to confirm the presence of free water in the outer capsule. The outer capsule was then opened and experiments where the sample capsule had obviously leaked silicate material during the run or where the alumina in the outer capsule was densely recrystallized were considered failures and were not analyzed further. In all successful experiments, we also confirmed the presence of nickel metal and nickel oxide in the platinum capsule. Experiments that appeared successful based on capsule evaluation were disqualified after further analysis if crystals were strongly zoned in major elements, had a mineral-melt FeO_{tot}-MgO $K_D > 0.40$ for olivine, or had a proportion of glass calculated by mass balance inconsistent with that of bracketing higher and lower temperature experiments. In this manuscript, we only report successful experiments.

Analytical Methods

The major element compositions of synthetic products were determined by electron probe microanalysis (EPMA). Analyses were performed on a JEOL JXA-8200 electron microprobe using five wavelength-dispersive spectrometers. The background correction method, analytical conditions, and analytical standards are identical to those described in Goltz et al. (2022). A time dependent intensity analysis was applied to glass analyses in experiment F174; the details of that correction are described in Goltz et al. (2022).

Results

General Observations

Observed phases in our experiments include olivine, clinopyroxene, orthopyroxene, amphibole, plagioclase, liquid (i.e., glass), and minor phosphates (**Table 2**). Crystal size varies from ~1μm to ~200μm, with clinopyroxene and minor phases usually among the smallest analyzed phases and amphibole and plagioclase among the largest. Crystals appear unzoned in major elements (Figure 1), except in experiment OD102 where crystals are zoned from core to rim in Mg and Fe (**Table 3**). Glass in all experiments is vesicular, and glass in H_2O-saturated experiments is also devitrified due to their high H_2O contents and difficulty quenching high pressure hydrous melts to glass (Gavrilenko et al., 2019).

Phase Relations

In this study, we conducted experiments at pressures of 500 MPa and 1 GPa and at temperatures ranging from 900-1205°C (Table 2). H_2O-saturated experiments have olivine as the liquidus phase, whereas the highest temperature runs in H_2O-undersaturated experiments contained ortho- and clino-pyroxene. Relatively higher temperature stability of plagioclase in H_2O-undersaturated experiments compared to H_2O-saturated runs is observed and was expected due to the suppression of plagioclase at high water contents (e.g., Sisson and Grove, 1993). Phase relations in all our experiments are tabulated in **Table 2**.

H_2O-Saturated Experiments

Olivine is the liquidus phase in high H_2O content experiments on the lo-K tephra starting compositions. In 1 GPa experiments on the lo-K tephra starting composition, clinopyroxene joins the equilibrium assemblage between 1075 and 1050°C. Between 1010 and 975°C at 1GPa, amphibole and orthopyroxene crystallize and olivine and clinopyroxene are no longer part of the crystallizing assemblage. Plagioclase crystallizes at temperatures below 925°C at 1GPa.

We did not determine the liquidus phase in H_2O-saturated experiments on the hi-K tephra starting compositions, but our highest temperature runs at 1050°C had equilibrium assemblages of olivine+clinopyroxene (mix 60) or olivine+clinopyroxene+amphibole (mix 53). In both starting compositions at 1 GPa, amphibole is present below 1025°C. At 0.5 GPa, amphibole is in equilibrium with melts below 1000°C.

H_2O-undersaturated, CO_2-free Experiments

Orthopyroxene+clinopyroxene±olivine are equilibrium phases in the highest temperature experiments at these conditions. Amphibole joins the equilibrium assemblage between 1100 and 1060°C in both starting compositions. Relative to H_2O-saturated experiments, amphibole joins the crystallizing assemblage at higher temperatures.

H_2O-undersaturated, Mixed-Volatile Experiments

Orthopyroxene±clinopyroxene are the equilibrium phases in the highest temperature experiments on mixed volatile experiments. In experiments on the lo-K tephra starting composition, plagioclase joins the crystallizing assemblage between 1100 and 1025°C at 1 GPa or between 1205 and 1055°C at 0.5 GPa. At 1025 °C at 1 GPa, amphibole joins the equilibrium assemblage; amphibole is not observed in experiments with mixed-volatiles at 0.5 GPa.

Phase Chemistry

The average chemistry of mineral phases and glass in our experiments is summarized in **Table 3**.

Olivine

Olivine in our experiments ranges from Fo_{76} to Fo_{88} (**Table 3**). The Fe-Mg K_D of olivine ranged from 0.25-0.39 (**Figure 2; Table 3**). The median The Fe-Mg K_D was 0.30, consistent with other experimentally determined values (e.g., Roeder and Emslie, 1970). The highest distribution coefficient is an outlier in our experiments (**Figure 2**). Besides its high olivine The Fe-Mg K_D, this experiment does not appear to be anomalous in the context of other experiments, and so we point it out specifically, but do not exclude it from our dataset. Olivine coexisting with amphibole ranged from Fo_{77} to Fo_{84}.

Amphibole

Amphibole in our experiments ranges from Mg# 66 to 84 (where Mg# is calculated $Mg/(Mg+Fe_{Tot})$ all in moles), in Al_2O_3 from 11 to 16 wt%, and in TiO_2 from 1.1-3.7 wt% (**Figure 3; Table 3**). Amphibole in the mixed volatile experiments have relatively high concentrations of TiO_2.

Clinopyroxene

Clinopyroxene ranges in Mg# from 75 to 87, and ranges in Al_2O_3 from 0.8 to 5.7 wt% (**Figure 4**). On average, clinopyroxene in mixed volatile experiments has higher Al_2O_3 than clinopyroxene in H_2O-saturated experiments. The Fe-Mg mineral-melt exchange coefficient (Fe-Mg K_D) for clinopyroxene ranges from 0.15 to 0.32, with a median value of 0.24 (**Figure 2**). The range of Fe-Mg K_D in our experiments is included within 2 standard deviations of the average clinopyroxene-melt Fe-Mg K_D calculated in Putirka (2008) (0.28 ± 0.16).

Orthopyroxene

Orthopyroxene in our experiments is most commonly observed in mixed volatile experiments as a near-liquidus phase, usually with clinopyroxene. It ranges from Mg# 61 to Mg# 87 (Figure 4; Table 3). Fe-Mg partitioning between orthopyroxene and melt ranges from 0.18 to 0.36 with a median value of 0.26 (**Figure 2**), all of which are within 2 s.d. of the average Fe-Mg K_D calculated by Putirka (2008) from 785 experimental points (0.29 ± 0.12).

Plagioclase

Plagioclase was present in seven of our experiments, six of which were run with mixed volatiles and one of which was run at H_2O-saturated conditions. The composition of the plagioclase ranged from An_{51} to An_{87}. The highest An plagioclase in our experiments was crystallized from the H_2O-saturated run, OD176, at our lowest experimental temperature, and was in equilibrium with amphibole of Mg# 66. Plagioclase with An_{52-54} was also found in equilibrium with amphibole (Mg# 67-69) in mixed volatile experiments.

Glass

In this section we examine the composition of glasses in our experiments with regard to trends in oxides with decreasing MgO. Glasses generally decrease in CaO and increase in SiO_2 with decreasing MgO, and there is significant overlap in the CaO and SiO_2 contents of glasses in mixed volatile, H_2O-undersaturated, and H_2O-saturated experiments (**Figure 5**). The Al_2O_3 content of glasses in mixed volatile experiments are lower than that of H_2O-saturated experiments at the same MgO. Glasses from amphibole-bearing H_2O-saturated experiments decrease in TiO_2 around 4 wt% MgO or lower; glasses from mixed volatile experiments maintain a constant TiO_2 with relatively low MgO and are higher in TiO_2 than glasses from H_2O-saturated experiments at the same MgO. Glasses in our H_2O-saturated experiments are low in alkalis relative to glasses from mixed volatile experiments, likely due to the preferential partitioning of these fluid-mobile elements into a free fluid phase.

Discussion

The primary goal of this study is to put constraints on the processes controlling the chemical evolution of the crustal magma system at Shiveluch Volcano, Kamchatka. We have conducted a suite of 47 high-pressure experiments on two primitive magmas erupted at Shiveluch and their derivatives. In order to draw conclusions, we directly compare the phase assemblages and phase compositions of our experiments to the whole rock compositions, phase assemblages, and phase compositions of basaltic tephra, mafic enclaves, and andesites erupted at Shiveluch. We find that the generation of andesites at Shiveluch requires some high-pressure differentiation of variably hydrated basalts in addition to other processes.

Conditions of Mid-to-Lower Crustal Storage at Shiveluch

Our approach in using experiments to constrain the conditions of mid to lower crustal crystallization at Shiveluch is similar to the approach used to determine the conditions of shallow intermediate magma storage prior to

explosive eruptions at volcanoes like Mt. St. Helens, Pinatubo, Santorini, Volcan Colima, Mascota, and Novarupta (e.g., Rutherford et al., 1985; Rutherford and Devine, 1996; Moore and Carmichael, 1998; Cottrell et al., 1999; Hammer et al., 2002; Prouteau and Scaillet, 2003). In those studies, P-T-X_{H2O} space was mapped for erupted compositions. The likely P-T-X_{H2O} of crystallization was determined by matching the observed phase assemblage in the erupted products to an area in the resulting phase diagram. Results were further refined and models given more complexity using phase chemistry, particularly of amphibole (e.g., Rutherford and Devine, 1988; Prouteau and Scaillet, 2003). These experiments were crucial, especially to relate the location of earthquakes to depths of shallow storage within the crust (e.g., Rutherford et al., 1985). Since then, the importance of lower crustal processes to volcanic behavior has been emphasized by models (e.g., Annen et al., 2006; Karakas et al., 2017; Glazner, 2021) and petrographic and geochemical observations (e.g., Davidson et al., 2007; Burns and de Silva, 2023). The lower crust is a fruitful area for study experimentally (e.g., Melekhova et al., 2015; Ulmer et al., 2018), and we explore lower crustal storage here in the context of Shiveluch, where mafic enclaves preserve near-liquidus phase assemblages and relatively undifferentiated magmatic compositions. In the case of the Shiveluch mafic enclaves, the target mineral assemblage is amphibole + olivine ± cpx. This is the near-liquidus assemblage in mafic enclaves and tephra, and minerals are accordingly high Mg# (Ol ≥ Fo_{88}, Amph ≥ Mg# 70, Cpx Mg# ≥ 80). In mafic enclaves, some high Mg# (i.e., Mg#≥74) amphibole is found as inclusions in high forsterite (Fo>88) olivine (Goltz et al., 2020).

The target assemblage (amph+ol±cpx) is relatively rare in the experimental literature. We used a compilation of phase equilibrium experiments from Weber and Blundy, 2024 to identify experiments containing equilibrium amphibole and olivine and compare them to our experimental products. The database of Weber and Blundy (2024) includes a summary of phase assemblages and published glass compositions normalized to 100. From a database of 2,546 experiments, only 74 experiments contain the key assemblage of amphibole + olivine (Supplementary Table 4). To these, we manually added published compositional information for cpx, ol, and amph where available; this compilation is available in supplementary table 4. Of the 74 experiments, 50% have plagioclase in their equilibrium assemblage, which is dissimilar to our target assemblage, and thus we do not discuss them further. All but one of the plagioclase-bearing experiments equilibrated at relatively low temperatures at or below 1000 °C and at or below 700 MPa. Of the 37 remaining plagioclase-free experiments, we exclude from discussion 10 additional experiments from Kelemen et al. (1990) and 7 experiments from Helz (1976) because amphibole in those experiments was not in equilibrium with melt at peak experimental conditions.

The remaining 20 plagioclase-free experiments provide an interesting window to the factors controlling amphibole stability in hydrous melts (Figure 6; Table 4). For example, experiments at upper crustal pressures (i.e., ≤300 MPa) where high Mg# amphibole and olivine are in equilibrium with mafic melt are from a higher alkali region of compositional space (Na_2O of basaltic starting compositions ranges from 3.97 to 4.59 wt%; Barclay and Carmichael 2004; Moore and Carmichael, 1998); enrichment in alkalis promotes amphibole stability at higher temperatures (Wallace and Green, 1991; Mandler and Grove, 2016), which likely contributed to the near-liquidus amphibole crystallization in these experiments. At mid-crustal pressures (300-700 MPa), high oxygen fugacities (up to NNO + 5) increased the liquidus temperature of amphibole, allowing it to be in equilibrium with high Mg# olivine (e.g., Krawczynski et al., 2012; Melekhova et al., 2015). At higher pressures, the effect of H_2O content is evident; all experiments with amphibole at 1 GPa are H_2O saturated, with the exception of experiment BM24 (Melekhova et al., 2015), which has a H_2O content of 9.3 wt%.

Our experiments—which show that amphibole and olivine are stable between 1000 and 1050°C at 1 GPa and H_2O saturated conditions (Table 2; Figure 6)—align well with the conditions of amphibole+olivine stability demonstrated in the literature, despite having different starting compositions and being run at a different oxygen fugacity. Taking into consideration our experimental results and results from experiments with broadly similar bulk compositions (Krawczynski et al., 2012; Melekhova et al., 2015; Ulmer et al., 2018), we bracket the conditions of high Mg# olivine and amphibole crystallization from mafic magmas at Shiveluch between 500 MPa and 1 GPa, and from 1000-1100 °C, with high (≥7.2 wt%) H_2O contents and at a range of oxygen fugacities. These conditions align with those estimated by microanalysis of minerals in mafic enclaves by Goltz et al. (2020).

The agreement between our experiments and results from the literature gives us confidence in and adds nuance to our results while exposing a fundamental problem with the experimental approach to creating new phase diagrams. Namely, there is no way to predict the extent to which we can accurately extrapolate between phase diagrams with multidimensional compositional differences in the presence of amphibole. A question we must address in coming years is: how similar is similar enough when we consider the effect of variations in compositional space on phase stability and composition? A combination of experimental and modeling efforts is required to constrain and fill gaps in the experimental literature through which extrapolation cannot be done accurately.

Processes Contributing to the Generation of Andesite at Shiveluch

Below, we compare mineral and melt compositions in our experiments to those observed in natural samples to elucidate the processes contributing to andesite genesis at Shiveluch.

Fractional Crystallization Plays a Role in Generating Andesite

The fractionation of phases crystallized in equilibrium with superhydrous magmas produces similar trends in major element oxides defined by andesites and mafic enclaves (with a noticeable exception of Al_2O_3, discussed below) extending to lower MgO (**Figure 5**). Specifically, we find that glass compositions in H_2O-saturated experiments that bear amphibole best reproduce the chemical trends in TiO_2 defined by whole rock compositions of andesites and mafic enclaves. In their study of mafic enclaves, Goltz et al. (2020) interpreted decreases in whole-rock TiO_2 and CaO with decreasing MgO starting at MgO ~4wt% as resulting from increased amphibole fractionation leading to compatible behavior of TiO_2.

Decreasing melt TiO_2 could be attributed to a change in the partitioning behavior of titanium between amphibole and melt or to the fractionation of more amphibole relative to other phases. We calculated the partition coefficient of titanium between amphibole and melt (D_{Ti}) for all amphibole-bearing experiments without normalizing amphibole compositions to 100. On average, the partition coefficient of titanium between amphibole and melt in our experiments is 2.7 ± 0.7. The partition coefficient is only weakly correlated with experimental temperature and is not correlated with H_2O content. The lowest H_2O content experiments containing amphibole do have the highest titanium content among amphiboles crystallized in this study by at least 1-2 weight percent (**Table 3**), but the amphibole-melt titanium partition coefficients (3.3 and 3.5) are within 2 s.d. of the average value. To summarize, the decrease in titanium observed in H_2O-saturated experiments containing amphibole is not associated with changes to the amphibole-melt titanium partition coefficient as a function of temperature (**Figure 7**). The trend in decreasing titanium observed in natural whole rock compositions thus indicates a necessary increase of amphibole percent in fractionated solids, in the absence of titanium-rich phases like ilmenite, which are not observed in mafic enclaves (Goltz et al., 2020).

The high proportion of amphibole in H_2O-saturated experiments causes them to decrease in TiO_2 with decreasing Mg#. The titanium content of the melt is negatively correlated with the percent of amphibole in the experiment among amphibole-bearing experiments (**Figure 7**). The implication of this finding is that the titanium content of a

melt in equilibrium with a high proportion of amphibole will decrease. In our experiments, such high proportions of amphibole only crystallize in experiments with very high (i.e., ≥10 wt%) H_2O contents, which indicates their importance in the production of andesite at Shiveluch.

Crustal Melting Also Contributes to the Generation of Andesites at Shiveluch

Although glasses in H_2O-saturated experiments reproduce the trend of decreasing TiO_2 observed in natural samples, glasses are much higher in Al_2O_3 than natural andesites (**Figure 5**). The enrichment of Al_2O_3 in glass synthesized from hydrous, high pressure experiments relative to andesites and dacites has been observed by others (e.g., Marxer et al., 2022; Marxer et al., 2023; Blatter et al., 2013; Blatter et al., 2017; Blatter et al., 2023) and is caused by the suppression of plagioclase at high H_2O contents (Sisson and Grove, 1993). While hydrous crystallization of basalt at upper crustal pressures (i.e., 100-200 MPa) produces glasses more similar in Al_2O_3 to natural andesites and dacites (e.g., Barclay and Carmichael, 2004; Rutherford et al., 1985; McCanta et al., 2007), these experiments do not produce the high Mg# amphibole and olivine assemblage from lower alkali content basalt that we observe in mafic enclaves, and thus this mechanism cannot work alone to produce intermediate arc lavas.

Others have invoked mixing in the upper and lower crust, crustal melting, and polybaric crystallization pathways to reconcile the high Al_2O_3 experimental melts with relatively low Al_2O_3 whole rock compositions, with various implications for crustal growth and delamination (Blatter et al., 2017; Rezeau et al., 2021; Marxer et al., 2022; Marxer et al., 2023; Blatter et al., 2023). The compositions of amphibole in mafic enclaves and experiments can help refine this list of hypotheses.

Generally, we find that the compositions of minerals in our experiments are similar to compositions observed in mafic enclaves (Figure 4). An important exception is the composition of amphiboles. At Mg# greater than ~70, amphiboles in Shiveluch mafic enclaves seem to define two groups: one with relatively high Al_2O_3 (11-12wt%) and one with relatively low Al_2O_3 (<10 wt%) (Figure 3). The groups converge at lower Mg# and higher Al_2O_3. At these Mg#, amphiboles in our experiments only overlap with the higher Al_2O_3 group. Similarly low Al_2O_3, high Mg# amphiboles have also been observed at Mt. Shasta (Krawczynski, 2011), Ciomadul (Cserep et al., 2023), and Mt. Pinatubo (Bernard et al., 1996; Rutherford and Devine, 1996).

One possibility to produce the low Al_2O_3, high Mg# amphiboles is crystallization of basalt at lower pressure. The Al-Tschermak's exchange in amphibole is widely recognized as a thermodynamic barometer for relatively silicic

melts (Blundy and Holland, 1990). For less silicic melts, Al^{VI} of amphibole has been empirically calibrated as a barometer (e.g., Ridolfi et al., 2010; Larocque and Canil, 2010; Krawczynski et al., 2012). Generally, amphibole crystallized at lower pressure should have lower Al^{VI} than an amphibole crystallized at higher pressures from a melt of identical composition. However, neither in low pressure (i.e., <500 MPa) equilibrium crystallization experiments with a basaltic starting composition (Marxer et al., 2023) nor in fractional crystallization-type experiments with a polybaric crystallization pathway (Marxer et al., 2022) do synthetic amphiboles overlap with the group of natural high Mg#, low Al_2O_3 amphiboles. Though shallow and polybaric crystallization pathways can produce lower Al_2O_3 melts, they cannot produce the lower Al_2O_3, high Mg# amphibole observed in mafic enclaves and thus may not be dominant processes at Shiveluch.

Mid-to-lower crustal crystallization from a hydrous dacitic melt is a more likely possibility to produce the high Mg#, low Al_2O_3 amphiboles. Some equilibrium experiments with dacitic starting compositions at mid-crustal conditions have produced amphibole with ≤10 wt% Al_2O_3 and Mg# ≥70 (Prouteau and Scaillet, 2003). All other elements held constant, low Al_2O_3 amphiboles are likely to be correspondingly high in SiO_2 to fill the tetrahedrally-coordinated site in the amphibole structure (i.e., T site; Hawthorne and Oberti, 2007) and so may be more likely to equilibrate with a relatively high SiO_2 melt. Crystallization of high Mg#, low Al_2O_3 amphibole from dacitic or adakitic melts in the lower crust produced via crustal melting and subsequent mixing with basalt (as proposed in Blatter et al., 2023) is a mechanism that could produce both low Al_2O_3, high Mg# amphibole and metaluminous andesite at Shiveluch. Trace elements in high Mg# amphibole with variable Al_2O_3 could be used to test this hypothesis.

Conclusions

Our experiments show that mid-to-lower crustal differentiation of a hydrous basalt is required to reproduce the near liquidus phase assemblage of amphibole+olivine±clinopyroxene observed in mafic enclaves at Shiveluch. We find that primitive magmas likely equilibrated with the observed near-liquidus assemblage between 500 MPa and 1 GPa, and from 1000-1100 °C, with high (≥7.2 wt%) H_2O contents, consistent with mineral geobarometry and thermometry (Goltz et al., 2020). However, this process cannot produce the metaluminous andesite erupted at Shiveluch and a group of low Al_2O_3, high Mg# amphibole alone. Using experimental data from the literature, we suggest that crystallization of and mixing of basalt with a hydrous dacite produced by melting of existing crust is also a key process in andesite production.

380

Figures and their captions

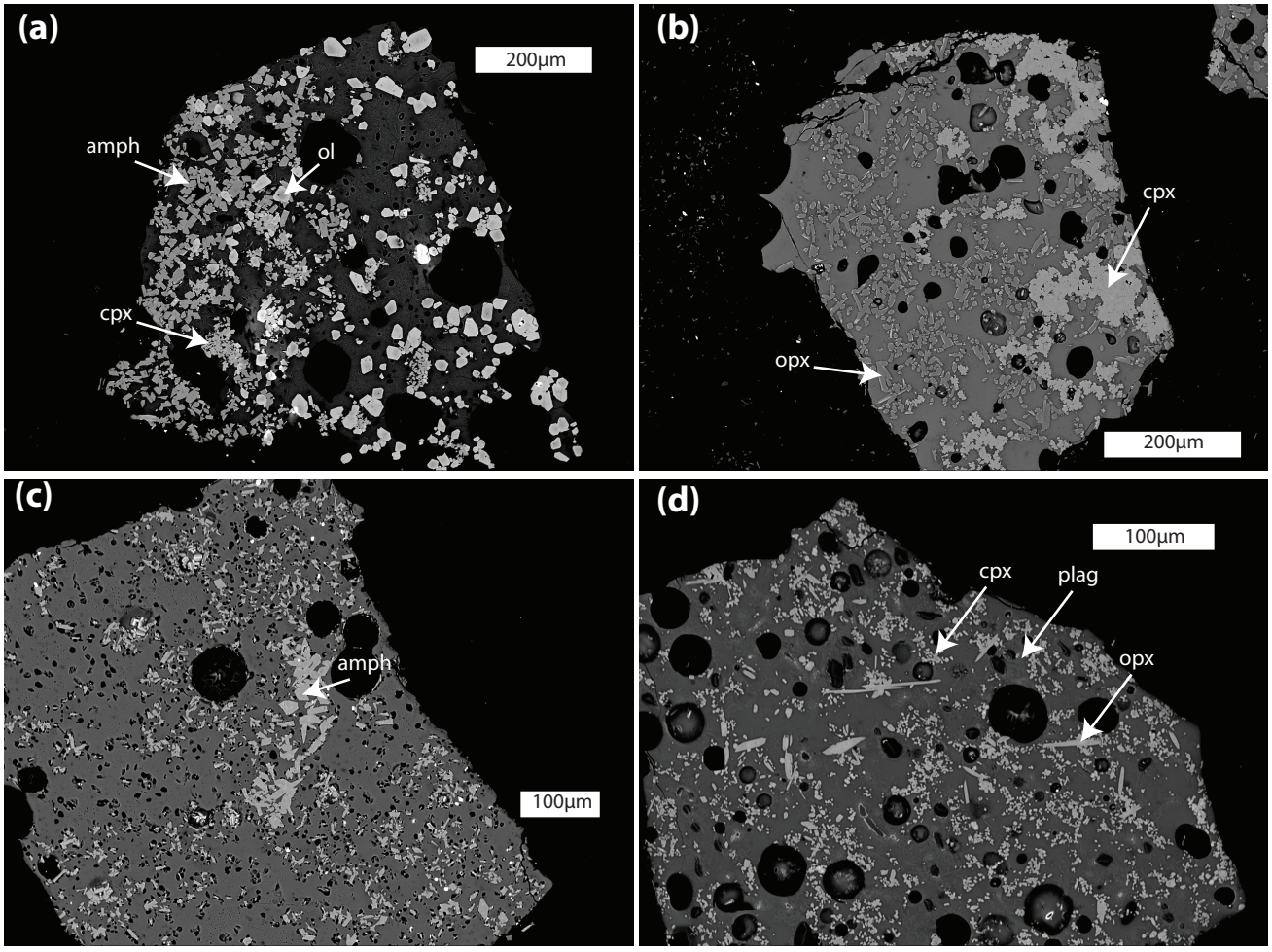

Figure 1. Back-scattered electron images of experiments (a) F136, (b) OD153, (c) F243, and (d) F242. Note frothy and vesiculated glass in water saturated experiments (a and c) as compared to glass in water undersaturated
385 experiments (b and d).

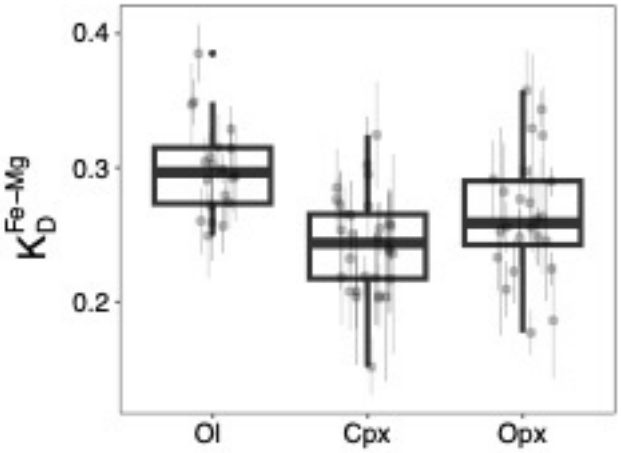

Figure 2. Mineral-melt Fe-Mg K_D for olivine, clinopyroxene, and orthopyroxene. Pale black points are average distribution coefficients for individual experiments; error bars are calculated by analytically propagating standard deviations of the average FeO and MgO of mineral and melt. Jitter around the x-axis is introduced for clarity only. Dark black point with a high value of olivine K_D indicates that it is an outlier by the definition of McGill et al. (1978). Box and whisker plots show the median (central thick black line), interquartile range (top and bottom of the box), and range of K_D for all experiments.

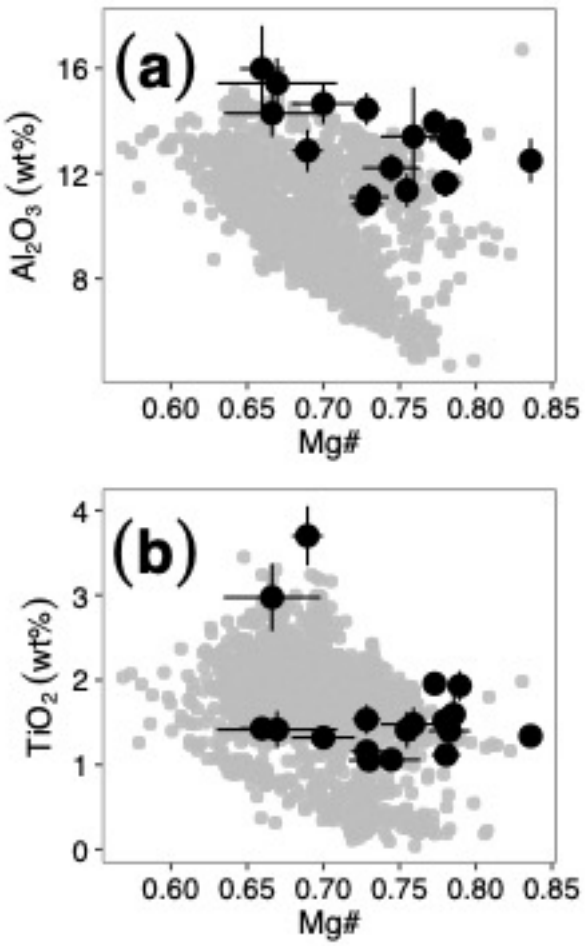

Figure 3. Mg# versus (a) Al_2O_3 and (b) TiO_2 of amphibole in our experiments (black points) and in Shiveluch mafic enclaves (grey points).

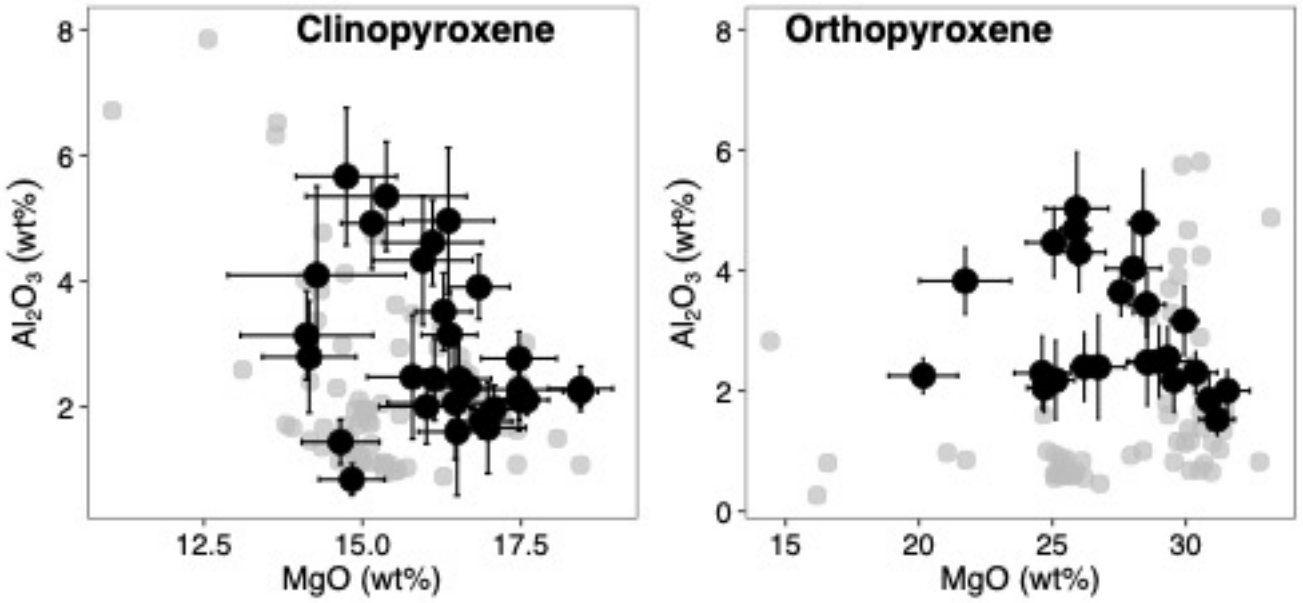

Figure 4. MgO vs Al_2O_3 of clinopyroxene and orthopyroxene in mafic enclaves (grey points) and experiments (black points).

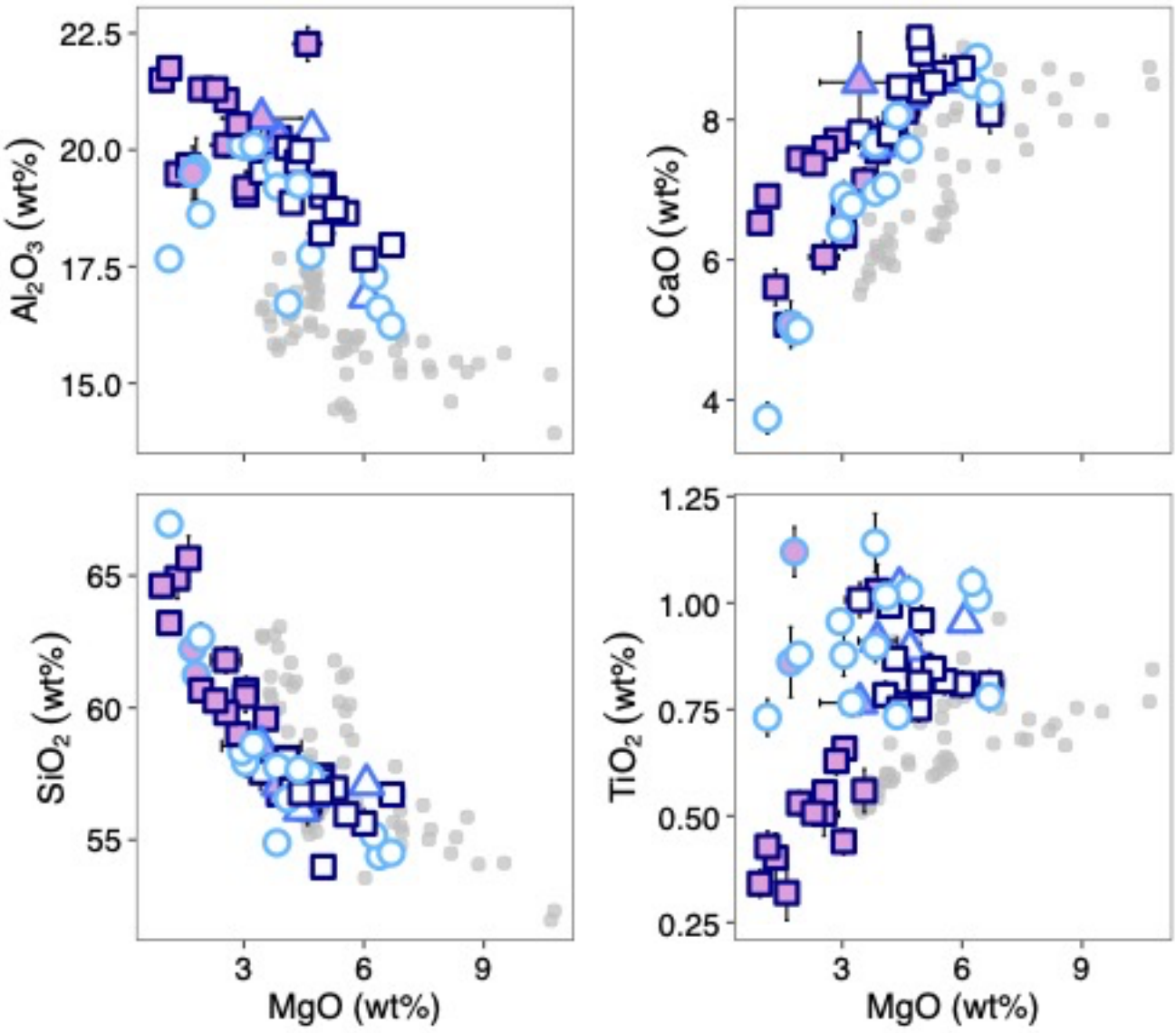

Figure 5. Compositional variation diagrams of experimental glasses and natural samples from Shiveluch. The color and shape of open shapes refers to the volatile content of the experiment containing that amphibole: dark blue squares are water saturated, periwinkle triangles are water undersaturated and lack CO_2, and light blue circles are water undersaturated with mixed volatiles. Points filled with pink represent experimental glasses in equilibrium with amphibole. Grey points are whole rock compositions of tephra, mafic enclaves, and andesites erupted from Shiveluch from Ponomareva et al. (2007), Goltz et al. (2020), Gorbach and Portnyagin (2011), Hochstaedter et al. (1996), Ishikawa et al. (2001), and Ferlito (2011).

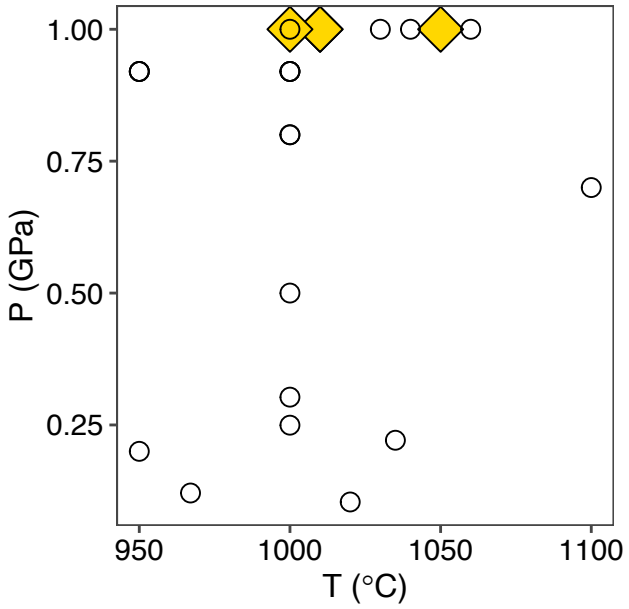

Figure 6. Pressure and temperature conditions of experiments with amphibole and olivine from this study (yellow diamonds) and the literature (open black circles). See Table 4 for more details on compiled amphibole- and olivine-bearing experiments from the literature.

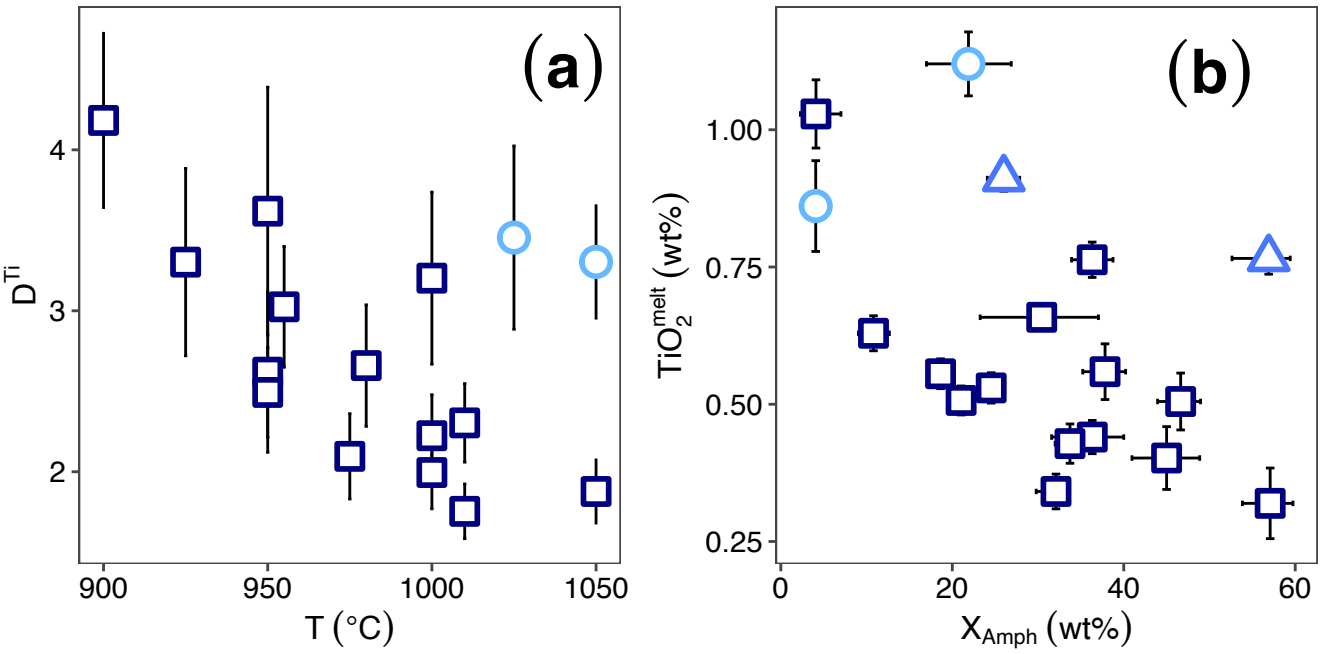

Figure 7. (a) Titanium partitioning between amphibole and melt (D_{Ti}) as a function of temperature. (b) Titanium content of experimental melt (TiO_{melt}) as a function of the proportion of amphibole in the experiment (X_{amph}). Colors and symbols are as in Figure 5.

Table Captions (tables follow references)

Table 1. Average compositions of experimental starting materials from repeated electron microprobe analysis. Sigma is the 1 standard deviation of the number of analyses ("no. analyses").

Table 2. Experimental run conditions. Phase proportions (in parentheses) were determined using the MATLAB program LIME (Prissel et al., 2023), and uncertainties can be found in Table 3 and Supplementary Tables 1 and 2. Fe loss was determined using the method presented in Prissel et al. (2023).

Table 3. Compositions and proportions of synthetic phases. Glass compositions are reported normalized to 100 with the un-normalized total. Numbers in italics are the 1 standard deviation of repeated analyses.

Table 4. Details of experiments with equilibrium amphibole + olivine from the compilation of Weber and Blundy (2024).

Supplementary Table Captions (submitted as .xlsx files and in GitHub)

Supplementary Table 1. Computer-readable datatable, including key compositional and run information. Columns 6-12 are "factor" columns where "1" indicates the phase is present and "0" indicates its absence. Data in this sheet is formatted to be easily compatible with the Weber and Blundy (2024) data scheme.

Supplementary Table 2. Expanded, computer-readable version of Table 2, including uncertainties on phase proportions.

Supplementary Table 3. Computer-readable version of Table 3.

Supplementary Table 4. Weber and Blundy (2024) experimental database filtered for experiments containing olivine and amphibole. The database includes information about the experimental run and the source of the compiled experiment in addition to the composition of glass. To this information, we added the compositions of amphibole, olivine, and clinopyroxene, where available.

Supplementary Table 5. Weber and Blundy (2024) experimental database filtered for experiments containing olivine and amphibole, without plagioclase.

Author contributions

A.E.G. conducted and analyzed experiments, synthesized data, compiled relevant literature data, and wrote and edited this manuscript. M.J.K. initially conceptualized this study, aided in data analysis, and edited the manuscript.

Acknowledgements

A.E.G. thanks Kelsey Prissel and Helene Couvy for their mentorship in and outside of the lab. A.E.G. acknowledges funding from the McDonnell Center for the Space Sciences at Washington University in St. Louis and from Carnegie Science. M.J.K. and A.E.G. acknowledge funding from NSF EAR grant #2042386 and M.J.K. acknowledges funding from NSF EAR grant #2047960.

Data availability

Computer-readable data for this manuscript is freely available at this GitHub repository.

References

Annen, C., Blundy, J. D., & Sparks, R. S. J. (2006). The genesis of intermediate and silicic magmas in deep crustal hot zones. Journal of Petrology, 47(3), 505–539. DOI: https://doi.org/10.1029/2023GC011234

Balta, J. B., Beckett, J. R., & Asimow, P. D. (2011). Thermodynamic properties of alloys of gold-74/palladium-26 with variable amounts of iron and the use of Au-Pd-Fe alloys as containers for experimental petrology. American Mineralogist, 96(10), 1467–1474. DOI: https://doi.org/10.2138/am.2011.3637

Barclay, J., & Carmichael, I. S. E. (2004). A hornblende basalt from western Mexico: water-saturated phase relations constrain a pressure–temperature window of eruptibility. Journal of Petrology, 45(3), 485–506. DOI: https://doi.org/10.1093/petrology/egg091

Barth, A., Portnyagin, M., Mironov, N., Holtz, F., Moussallam, Y., Rose-Koga, E. F., Rasmussen, D., Towbin, H., Gonnermann, H., & Mutch, E. J. F. (2024). Fast, furious, and gassy: Etna's explosive eruption from the mantle. Earth and Planetary Science Letters, 643, 118864. DOI: https://doi.org/10.1016/j.epsl.2024.118864

Bernard, A., Knittel, U., Weber, B., Weis, D., Albrecht, A., Hattori, K., Klein, J., & Oles, D. (1996). Petrology and geochemistry of the 1991 eruption products of Mount Pinatubo. Fire and Mud: Eruptions and Lahars of Mount Pinatubo, Philippines, 767–797.

Blatter, D. L., Sisson, T. W., & Hankins, W. B. (2013). Crystallization of oxidized, moderately hydrous arc basalt at mid-to lower-crustal pressures: implications for andesite genesis. Contributions to Mineralogy and Petrology, 166, 861–886. DOI: https://doi.org/10.1007/s00410-013-0920-3

Blatter, D. L., Sisson, T. W., & Hankins, W. B. (2017). Voluminous arc dacites as amphibole reaction-boundary liquids. Contributions to Mineralogy and Petrology, 172, 1–37. DOI: https://doi.org/10.1007/s00410-017-1340-6

Blatter, D. L., Sisson, T. W., & Hankins, W. B. (2023). Garnet stability in arc basalt, andesite, and dacite—an experimental study. Contributions to Mineralogy and Petrology, 178(6), 33. DOI: https://doi.org/10.1007/s00410-023-02008-w

Burns, D. H., & de Silva, S. L. (2023). Andesites and evolution of the continental crust: Perspectives from the Central Volcanic Zone of the Andes. Frontiers in Earth Science, 10, 961130. DOI: https://doi.org/10.3389/feart.2022.961130

Cottrell, E., Gardner, J. E., & Rutherford, M. J. (1999). Petrologic and experimental evidence for the movement and heating of the pre-eruptive Minoan rhyodacite (Santorini, Greece). Contributions to Mineralogy and Petrology, 135(4), 315–331. DOI: https://doi.org/10.1007/s004100050514

Cserép, B., Szemerédi, M., Harangi, S., Erdmann, S., Bachmann, O., Dunkl, I., Seghedi, I., Mészáros, K., Kovács, Z., & Virág, A. (2023). Constraints on the pre-eruptive magma storage conditions and magma evolution of the 56–30 ka explosive volcanism of Ciomadul (East Carpathians, Romania). Contributions to Mineralogy and Petrology, 178(12), 96. DOI: https://doi.org/10.1007/s00410-023-02075-z

Davidson, J., Turner, S., Handley, H., Macpherson, C., & Dosseto, A. (2007). Amphibole "sponge" in arc crust? Geology, 35(9), 787–790. DOI: https://doi.org/10.1130/G23637A.1

Dayton, K., Gazel, E., Wieser, P., Troll, V. R., Carracedo, J. C., la Madrid, H., Roman, D. C., Ward, J., Aulinas, M., & Geiger, H. (2023). Deep magma storage during the 2021 La Palma eruption. Science Advances, 9(6), eade7641. DOI: 10.1126/sciadv.ade7641

Ferlito, C. (2011). Bimodal geochemical evolution at Sheveluch stratovolcano, Kamchatka, Russia: consequence of a complex subduction at the junction of the Kuril Kamchatka and Aleutian island arcs. Earth-Science Reviews, 105(1–2), 49–69. DOI: https://doi.org/10.1016/j.earscirev.2010.12.003

Gavrilenko, M., Krawczynski, M., Ruprecht, P., Li, W., & Catalano, J. G. (2019). The quench control of water estimates in convergent margin magmas. American Mineralogist, 104(7), 936–948. DOI: https://doi.org/10.2138/am-2019-6735

Glazner, A. F. (2021). Thermal constraints on the longevity, depth, and vertical extent of magmatic systems. Geochemistry, Geophysics, Geosystems, 22(4), e2020GC009459. DOI: https://doi.org/10.1029/2020GC009459

Global Volcanism Program, 2024. [Database] Volcanoes of the World (v. 5.2.8; 6 May 2025). Distributed by Smithsonian Institution, compiled by Venzke, E. DOI: https://doi.org/10.5479/si.GVP.VOTW5-2024.5.2

Goltz, A. E., Krawczynski, M. J., Gavrilenko, M., Gorbach, N. v, & Ruprecht, P. (2020). Evidence for superhydrous primitive arc magmas from mafic enclaves at Shiveluch volcano, Kamchatka. Contributions to Mineralogy and Petrology, 175, 1–26. DOI: https://doi.org/10.1007/s00410-020-01746-5

Goltz, A. E., Krawczynski, M. J., McCanta, M. C., & Darby Dyar, M. (2022). Experimental calibration of an Fe3+/Fe2+-in-amphibole oxybarometer and its application to shallow magmatic processes at Shiveluch Volcano, Kamchatka. American Mineralogist, 107(11), 2084–2100. DOI: https://doi.org/10.2138/am-2022-8031

Gorbach, N. V., & Portnyagin, M. (2011). Geology and Petrology of the Lava Complex of Young Shiveluch Volcano, Kamchatka. Petrology, 19(2), 134–166. DOI: https://doi.org/10.1134/S0869591111020068

Gualda, G. A. R., Ghiorso, M. S., Lemons, R. v, & Carley, T. L. (2012). Rhyolite-MELTS: a modified calibration of MELTS optimized for silica-rich, fluid-bearing magmatic systems. Journal of Petrology, 53(5), 875–890. DOI: https://doi.org/10.1093/petrology/egr080

Hammer, J. E., Rutherford, M. J., & Hildreth, W. (2002). Magma storage prior to the 1912 eruption at Novarupta, Alaska. Contributions to Mineralogy and Petrology, 144, 144–162. DOI: https://doi.org/10.1007/s00410-002-0393-2

Harmon, L. J., Gualda, G. A. R., Gravley, D. M., Smithies, S. L., & Deering, C. D. (2024). The Whakamaru magmatic system (Taupō Volcanic Zone, New Zealand), part 1: Evidence from tephra deposits for the eruption of multiple magma types through time. Journal of Volcanology and Geothermal Research, 445, 107966. DOI: https://doi.org/10.1016/j.jvolgeores.2023.107966

Hawthorne, F. C., & Oberti, R. (2007). Amphiboles: Crystal Chemistry. In Amphiboles (pp. 1–54). De Gruyter. DOI: https://doi.org/10.1515/9781501508523-002

Helz, R. T. (1976). Phase relations of basalts in their melting ranges at P H2O= 5 kb. Part II. Melt compositions. Journal of Petrology, 17(2), 139–193. DOI: https://doi.org/10.1093/petrology/17.2.139

Hochstaedter, A. G., Kepezhinskas, P., Defant, M., Drummond, M., & Koloskov, A. (1996). Insights into the volcanic arc mantle wedge from magnesian lavas from the Kamchatka arc. Journal of Geophysical Research: Solid Earth, 101(B1), 697–712. DOI: https://doi.org/10.1029/95JB02404

Ishikawa, T., Tera, F., & Nakazawa, T. (2001). Boron isotope and trace element systematics of the three volcanic zones in the Kamchatka arc. Geochimica et Cosmochimica Acta, 65(24), 4523–4537. DOI: https://doi.org/10.1016/S0016-7037(01)00765-7

Karakas, O., Degruyter, W., Bachmann, O., & Dufek, J. (2017). Lifetime and size of shallow magma bodies controlled by crustal-scale magmatism. Nature Geoscience, 10(6), 446–450. DOI: https://doi.org/10.1038/ngeo2959

Kelemen, P. B., Joyce, D. B., Webster, J. D., & Holloway, J. R. (1990). Reaction between ultramafic rock and fractionating basaltic magma II. Experimental investigation of reaction between olivine tholeiite and harzburgite at 1150–1050 C and 5 kb. Journal of Petrology, 31(1), 99–134. DOI: https://doi.org/10.1093/petrology/31.1.99

Krawczynski, M. J. (2011). Experimental studies of melting and crystallization processes in planetary interiors.

Krawczynski, M. J., Grove, T. L., & Behrens, H. (2012). Amphibole stability in primitive arc magmas: effects of temperature, H2O content, and oxygen fugacity. Contributions to Mineralogy and Petrology, 164(2), 317–339. DOI: https://doi.org/10.1007/s00410-012-0740-x

Larocque, J., & Canil, D. (2010). The role of amphibole in the evolution of arc magmas and crust: the case from the Jurassic Bonanza arc section, Vancouver Island, Canada. Contributions to Mineralogy and Petrology, 159, 475–492. DOI: https://doi.org/10.1007/s00410-009-0436-z

Mandler, B. E., & Grove, T. L. (2016). Controls on the stability and composition of amphibole in the Earth's mantle. Contributions to Mineralogy and Petrology, 171, 1–20. DOI: https://doi.org/10.1007/s00410-016-1281-5

Marxer, F., Ulmer, P., & Müntener, O. (2022). Polybaric fractional crystallisation of arc magmas: an experimental study simulating trans-crustal magmatic systems. Contributions to Mineralogy and Petrology, 177(1), 3. DOI: https://doi.org/10.1007/s00410-021-01856-8

Marxer, F., Ulmer, P., & Müntener, O. (2023). Ascent-driven differentiation: a mechanism to keep arc magmas metaluminous? Contributions to Mineralogy and Petrology, 178(8), 51. DOI: https://doi.org/10.1007/s00410-023-02035-7

McCanta, M. C., Rutherford, M. J., & Hammer, J. E. (2007). Pre-eruptive and syn-eruptive conditions in the Black Butte, California dacite: Insight into crystallization kinetics in a silicic magma system. Journal of Volcanology and Geothermal Research, 160(3–4), 263–284. DOI: https://doi.org/10.1016/j.jvolgeores.2006.10.004

McGill, R., Tukey, J. W., & Larsen, W. A. (1978). Variations of box plots. The American Statistician, 32(1), 12–16. DOI: https://doi.org/10.1080/00031305.1978.10479236

Moore, G., & Carmichael, I. S. E. (1998). The hydrous phase equilibria (to 3 kbar) of an andesite and basaltic andesite from western Mexico: constraints on water content and conditions of phenocryst growth. Contributions to Mineralogy and Petrology, 130(3), 304–319. DOI: https://doi.org/10.1007/s004100050367

Nandedkar, R. H., Ulmer, P., & Müntener, O. (2014). Fractional crystallization of primitive, hydrous arc magmas: an experimental study at 0.7 GPa. Contributions to Mineralogy and Petrology, 167(6), 1015. DOI: https://doi.org/10.1007/s00410-014-1015-5

Pamukcu, A. S., Gualda, G. A. R., Ghiorso, M. S., Miller, C. F., & McCracken, R. G. (2015). Phase-equilibrium geobarometers for silicic rocks based on rhyolite-MELTS—Part 3: Application to the Peach Spring Tuff (Arizona–California–Nevada, USA). Contributions to Mineralogy and Petrology, 169, 1–17. DOI: https://doi.org/10.1007/s00410-015-1122-y

Ponomareva, V., Melekestsev, I., Braitseva, O., Churikova, T., Pevzner, M., & Sulerzhitsky, L. (2007). Late Pleistocene-Holocene volcanism on the Kamchatka Peninsula, Northwest Pacific Region (pp. 165–198). DOI: https://doi.org/10.1029/172GM15

Prissel, K., Olive, J., & Krawczynski, M. J. (2023). A log-ratio-based algorithm for petrologic mass-balance problems and uncertainty assessment. Geochemistry, Geophysics, Geosystems, 24(12), e2023GC011234. DOI: https://doi.org/10.1029/2023GC011234

Prouteau, G., & Scaillet, B. (2003). Experimental constraints on the origin of the 1991 Pinatubo dacite. Journal of Petrology, 44(12), 2203–2241. DOI: https://doi.org/10.1093/petrology/egg075

Putirka, K. D. (2008). Thermometers and barometers for volcanic systems. Reviews in Mineralogy and Geochemistry, 69(1), 61–120. DOI: https://doi.org/10.2138/rmg.2008.69.3

Rezeau, H., Klein, B. Z., & Jagoutz, O. (2021). Mixing dry and wet magmas in the lower crust of a continental arc: new petrological insights from the Bear Valley Intrusive Suite, southern Sierra Nevada, California. Contributions to Mineralogy and Petrology, 176(9), 73. DOI: https://doi.org/10.1007/s00410-021-01832-2

Ridolfi, F., Renzulli, A., & Puerini, M. (2010). Stability and chemical equilibrium of amphibole in calc-alkaline magmas: an overview, new thermobarometric formulations and application to subduction-related volcanoes. Contributions to Mineralogy and Petrology, 150, 45–66. DOI: https://doi.org/10.1007/s00410-009-0465-7

Roeder, P. L., & Emslie, Rf. (1970). Olivine-liquid equilibrium. Contributions to Mineralogy and Petrology, 29(4), 275–289. DOI: https://doi.org/10.1007/BF00371276

Rutherford, M. J., & Devine, J. D. (1988). The May 18, 1980, eruption of Mount St. Helens: 3. Stability and chemistry of amphibole in the magma chamber. Journal of Geophysical Research: Solid Earth, 93(B10), 11949–11959. DOI: https://doi.org/10.1029/JB093iB10p11949

Rutherford, M. J., & Devine, J. D. (1996). Preeruption pressure-temperature conditions and volatiles in the 1991 dacitic magma of Mount Pinatubo. Fire and Mud: Eruptions and Lahars of Mount Pinatubo, Philippines, 751–766.

Rutherford, M. J., Sigurdsson, H., Carey, S., & Davis, A. (1985). The May 18, 1980, eruption of Mount St. Helens: 1. Melt composition and experimental phase equilibria. Journal of Geophysical Research: Solid Earth, 90(B4), 2929–2947. DOI: https://doi.org/10.1029/JB090iB04p02929

Sisson, T. W., & Grove, T. L. (1993). Experimental investigations of the role of H 2 O in calc-alkaline differentiation and subduction zone magmatism. Contributions to Mineralogy and Petrology, 113, 143–166. DOI: https://doi.org/10.1007/BF00283225

Sisson, T. W., Ratajeski, K., Hankins, W. B., & Glazner, A. F. (2005). Voluminous granitic magmas from common basaltic sources. Contributions to Mineralogy and Petrology, 148, 635–661. DOI: https://doi.org/10.1007/s00410-004-0632-9

Till, C. B., Kent, A. J. R., Abers, G. A., Janiszewski, H. A., Gaherty, J. B., & Pitcher, B. W. (2019). The causes of spatiotemporal variations in erupted fluxes and compositions along a volcanic arc. Nature Communications, 10(1), 1350. DOI: https://doi.org/10.1007/s00410-004-0632-9

Ulmer, P., Kaegi, R., & Müntener, O. (2018). Experimentally derived intermediate to silica-rich arc magmas by fractional and equilibrium crystallization at 1· 0 GPa: an evaluation of phase relationships, compositions, liquid

lines of descent and oxygen fugacity. Journal of Petrology, 59(1), 11–58. DOI: https://doi.org/10.1093/petrology/egy017

Volynets, O. N., Ponomareva, V. v, & Babansky, A. D. (1997). Magnesian basalts of Shiveluch andesite volcano, Kamchatka. Petrology, 5(2), 206–221.

Wallace, M., & Green, D. H. (1991). The effect of bulk rock composition on the stability of amphibole in the upper mantle: implications for solidus positions and mantle metasomatism. Mineralogy and Petrology, 44(1–2), 1–19. DOI: 10.1007/BF01167097

Weber, G., & Blundy, J. (2024). A machine learning-based thermobarometer for magmatic liquids. Journal of Petrology, 65(4), egae020. DOI: https://doi.org/10.1093/petrology/egae020

Wieser, P. E., Kent, A. J. R., Till, C. B., & Abers, G. A. (2023). Geophysical and geochemical constraints on magma storage depths along the Cascade arc: knowns and unknowns. Geochemistry, Geophysics, Geosystems, 24(11), e2023GC011025. DOI: https://doi.org/10.1029/2023GC011025

Wieser, P., Petrelli, M., Lubbers, J., Wieser, E., Ozaydin, S., Kent, A., & Till, C. (2022). Thermobar: An open-source Python3 tool for thermobarometry and hygrometry. Volcanica, 5(2), 349–384. DOI: https://doi.org/10.30909/vol.05.02.349384

Table 1. Average compositions of experimental starting materials from repeated electron microprobe analysis. Sigma is the 1 standard deviation of the number of analyses ("no. analyses").

Mix no. and description	53-hiK Tephra Parent		60-hiK Tephra		70-mixed volatile hiK Tephra		54-loK Tephra Parent		59-loK Tephra		73-Mixed volatile loK Tephra		76-Evolved loK tephra		79-Mixed volatile evolved loK Tephra	
No. Analyses	10		38		5		16		51		18		10		9	
	Average	σ	Average	σ	Average	σ	Average	σ	Average	σ	Average	σ	Average	σ	Average	σ
SiO2	52.80	0.83	52.54	0.39	55.13	0.84	52.10	0.27	54.02	1.01	55.62	0.71	55.03	1.84	57.36	1.85
TiO2	0.77	0.04	0.81	0.03	0.79	0.02	0.62	0.03	0.75	0.04	0.76	0.04	0.73	0.03	0.75	0.03
Al2O3	12.86	0.08	13.73	0.11	13.66	0.42	12.71	0.05	16.04	0.43	15.11	0.37	19.86	1.20	18.24	1.09
FeO	8.20	0.12	8.64	0.13	7.06	0.60	8.03	0.07	7.50	0.37	7.30	0.19	6.06	0.42	5.62	0.54
MnO	0.20	0.01	0.20	0.02	0.20	0.02	0.17	0.02	0.19	0.01	0.15	0.01	0.22	0.02	0.20	0.01
MgO	13.19	0.14	10.84	0.10	9.90	0.28	16.32	0.10	9.49	0.22	8.61	0.16	5.03	0.27	4.37	0.12
CaO	7.83	0.07	8.51	0.08	8.48	0.25	6.56	0.05	7.89	0.17	7.77	0.16	8.44	0.43	7.83	0.39
Na2O	2.66	0.05	2.74	0.04	2.72	0.06	2.76	0.03	3.26	0.10	3.57	0.07	3.52	0.16	4.34	0.11
K2O	1.49	0.04	1.64	0.03	1.59	0.08	0.55	0.02	0.66	0.04	0.91	0.03	0.82	0.07	0.99	0.06
P2O5	0.02	0.02	0.36	0.03	0.46	0.03	0.21	0.02	0.21	0.03	0.22	0.02	0.31	0.02	0.33	0.03

Table 2. Experimental run conditions. Phase proportions (in parentheses) were determined using the MATLAB program LIME (Prissel et al., 2023), and uncertainties can be found in Table 3 and Supplementary Tables 1 and 2. Fe loss was determined using the method presented in Prissel et al. (2023).

ID	Starting mix no.	T (°C)	P (GPa)	Duration (hrs)	Water added (bulk)	Equilibrium assemblage	Capsule Material	Iron loss to capsule (%)
F136	53	1010	1	46.97	Saturated	g(46)+ol(11)+cpx(12)+amph(30)	Au	2.43
OD102	53	1050	1	47.30	Saturated	g(59)+ol*(18)+cpx(19)+amph(4)	Au	-5.03
F149	60	950	1	49.47	Saturated	g(47)+opx(8)+amph(45)+ap(3)	Au	-7.26
F163	60	1000	1	47.73	Saturated	g(49)+ol(3)+cpx(9)+opx(3)+amph(36)	Au	-10.7
OD173	60	1025	1	24.03	Saturated	g(70)+ol(10)+cpx(20)	Au	-11.9
F153	60	1050	1	48.53	Saturated	g(73)+ol(11)+cpx(16)	Au	-13.4
F174	60	950	0.5	47.57	Saturated	g(39)+opx(3)+amph(57)+ap(1)	Au	-6.15
F175	60	1000	0.5	48.60	Saturated	g(68)+ol(12)+cpx(20)	Au	-14.1
OD143	60	1060	1	46.90	6 wt%	g(46)+cpx(22)+opx(6)+amph(26)	Au	-11.4
F204	60	1075	1	27.07	6 wt%	g(70)+ol(9)+cpx(19)+opx(2)	Au	-14.9
OD141	60	1100	1	47.57	6 wt%	g(75)+ol(8)+cpx(15)+opx(2)	Au	-19.6
OD155	70	1105	1	26.27	3 wt%	g(64)+cpx(21)+opx(15)	Au80Pd20	5.5
OD153	70	1140	1	23.90	3 wt%	g(78)+cpx(11)+opx(11)	Au80Pd20	-9.03
OD150	70	1175	1	24.05	3 wt%	g(79)+cpx(10)+opx(11)	Au80Pd20	5.11
F230	70	1080	0.5	12.20	3 wt%	g(75)+ol(5)+cpx(13)+opx(7)	Au	-11.7
F137	54	1010	1	47.30	Saturated	g(42)+ol(22)+amph(36)	Au	-0.59
F145	54	1050	1	23.83	Saturated	g(61)+ol(26)+cpx(13)	Au	-10.6
F125	54	1100	1	24.17	Saturated	g(76)+ol(24)	Au	-7.67
OD168	59	975	1	22.97	Saturated	g(51)+opx(2)+amph(47)	Au	4.4
OD109	59	1000	1	51.97	Saturated	g(59)+opx(3)+amph(38)	Au	-1.96
OD166	59	1010	1	21.87	Saturated	g(77)+ol(9)+cpx(14)	Au	-4.48
OD160	59	1025	1	29.03	Saturated	g(77)+ol(9)+cpx(14)	Au	-11.9
OD161	59	1050	1	43.20	Saturated	g(83)+ol(10)+cpx(8)	Au	-13.7
OD167	59	1075	1	23.03	Saturated	g(90)+ol(10)	Au	-3.59
OD163	59	1100	1	24.03	Saturated	g(91)+ol(9)	Au	-5.35
OD144	59	1060	1	47.03	6 wt%	g(40)+cpx(1)+opx(2)+amph(57)	Au	-9.66
OD142	59	1100	1	47.87	6 wt%	g(75)+cpx(14)+opx(11)	Au	-15.1
OD169	73	1050	1	18.92	3 wt%	g(46)+cpx(12)+opx(11)+amph(22)+plag(9)	Au	1.02
OD171	73	1075	1	19.07	3 wt%	g(69)+cpx(13)+opx(16)+plag(2)	Au	-10.9
OD170	73	1100	1	19.90	3 wt%	g(75)+cpx(10)+opx(15)	Au80Pd20	-0.3
OD172	73	1125	1	21.20	3 wt%	g(76)+cpx(9)+opx(16)	Au80Pd20	-9.09
F233	59	1055	0.5	12.27	Saturated	g(89)+ol(11)	Au	-0.19
F228	59	1080	0.5	12.30	Saturated	g(91)+ol(9)	Au	-7.81
F236	73	1155	0.5	13.00	3 wt%	g(55)+cpx(10)+opx(17)+plag(18)	Au80Pd20	4.17
F231	73	1205	0.5	13.03	3 wt%	g(92)+opx(8)	Au80Pd20	17.3
F246	76	955	0.5	21.30	Saturated	g(79)+amph(21)	Au	-9.19
F243	76	980	0.5	21.97	Saturated	g(81)+amph(19)	Au	-9.75
F237	76	1030	0.5	12.27	Saturated	g(96)+ol(1)+cpx(3)	Au	-7.34
OD176	76	900	1	24.13	Saturated	g(65)+amph(32)+plag(3)	Au	-13.2
OD179	76	925	1	21.32	Saturated	g(66)+amph(34)	Au	-4.73
OD175	76	950	1	22.20	Saturated	g(75)+amph(25)	Au	-0.71
OD174	76	1000	1	24.23	Saturated	g(87)+cpx(2)+amph(11)	Au	-9.52
OD177	79	1025	1	24.27	3 wt%	g(33)+cpx(8)+opx(9)+amph(4)+plag(46)	Au	-17.4
OD178	79	1075	1	22.80	3 wt%	g(94)+cpx(4)+opx(2)	Au	-10.3
F245	79	980	0.5	21.60	3 wt%	g(55)+cpx(19)+opx(5)+plag(21)	Au	-20.78
F242	79	1005	0.5	22.17	3 wt%	g(62)+cpx(16)+opx(4)+plag(18)	Au	-8.95
F241	79	1055	0.5	19.60	3 wt%	g(100)	Au	-20.1

Table 3. Compositions and proportions of synthetic phases. Glass compositions are reported normalized to 100 with the un-normalized total. Numbers in italics are the 1 standard deviation of repeated analyses.

Run No.	Phase	No. Analyses	Proportion (-25%/+75%)	SiO2		TiO2		Al2O3		FeO		MnO		MgO		CaO		Na2O		K2O		P2O5		Total	Mg #	KD Fe-Mg	D Ti
F136	g	17	46.0 (-0.9/+3.5)	60.67	*0.5*	0.66	*0.02*	19.04	*0.17*	6	*0.11*	0.17	*0.02*	3.06	*0.22*	6.35	*0.21*	1.9	*0.29*	2.13	*0.15*	0.03	*0.02*	88.9	0.48		
	ol	17	11.4 (-1.0/+1.5)	39.1	*0.73*	0.03	*0.01*	0.02	*0.01*	20.44	*1.1*	0.41	*0.03*	39.98	*1.11*	0.15	*0.05*	BDL	-	BDL	-	BDL	-	100.15	0.78	0.26	
	cpx	19	12.1 (-4.9/+3.8)	53.03	*0.71*	0.43	*0.1*	2.44	*0.66*	6.89	*0.59*	0.27	*0.06*	16.14	*0.45*	20.88	*0.73*	0.36	*0.21*	0.03	*0.01*	0.02	*0.01*	100.48	0.81	0.22	
	amph	22	30.4 (-6.6/+7.2)	44.62	*0.43*	1.52	*0.15*	11.63	*0.5*	8.3	*0.17*	0.15	*0.01*	16.44	*0.34*	11.43	*0.22*	2.14	*0.05*	0.93	*0.05*	BDL	-	97.15	0.78	0.26	2.3
OD102	g	20	58.8 (-0.4/+3.0)	56.73	*0.28*	1.03	*0.06*	20.25	*0.14*	5.96	*0.15*	0.16	*0.03*	3.88	*0.18*	7.55	*0.1*	2.41	*0.17*	2.02	*0.2*	BDL	-	88.47	0.54		
	ol (rims)	11	4.8 (-2.4/+1.7)	38.74	*0.5*	0.03	*0.01*	BDL	-	19.35	*0.41*	0.38	*0.02*	40.93	*0.77*	0.13	*0.02*	BDL	-	BDL	-	BDL	-	99.57	0.79	0.31	
	ol (cores)	12	13.0 (-1.9/+2.2)	39.85	*0.52*	0.06	*0.03*	0.04	*0.04*	15.11	*1.69*	0.36	*0.02*	44.58	*1.6*	0.2	*0.1*	BDL	-	BDL	-	0.02	*0.02*	100.24	0.84	0.22	
	cpx	13	19.3 (-0.6/+1.5)	52.89	*0.86*	0.41	*0.04*	2.32	*0.24*	5.61	*0.25*	0.2	*0.02*	16.67	*0.39*	22.03	*0.41*	0.27	*0.08*	0.02	*0.01*	BDL	-	100.42	0.84	0.22	
	amph	10	4.1 (-2.9/+1.8)	43.33	*0.7*	1.93	*0.18*	12.96	*0.6*	7.89	*0.15*	0.16	*0.01*	16.6	*0.64*	11.42	*0.12*	2.36	*0.1*	0.83	*0.05*	0.02	*0.02*	97.5	0.79	0.31	1.9
F149	g	17	46.6 (-1.4/+2.1)	64.9	*0.77*	0.4	*0.06*	19.49	*0.27*	4.72	*0.52*	0.16	*0.03*	1.34	*0.27*	5.61	*0.26*	0.69	*0.21*	2.1	*0.11*	0.59	*0.03*	86.88	0.33		
	opx	15	8.4 (-2.4/+1.9)	53.62	*0.77*	0.16	*0.04*	2.18	*0.66*	16.52	*0.53*	0.48	*0.05*	25.12	*0.7*	1.55	*0.21*	0.02	*0.02*	0.02	*0*	BDL	-	99.68	0.73	0.19	
	amph	18	45 (-3.9/+4.0)	45.71	*0.58*	1.05	*0.13*	11.1	*0.52*	10.51	*0.46*	0.24	*0.04*	15.94	*0.54*	10.63	*0.5*	1.89	*0.08*	0.72	*0.14*	0.05	*0.03*	97.83	0.73	0.19	2.6
	ap	7	3.1 (-0.5/+0.5)	0.47	*0.27*	BDL	-	0.04	*0.04*	0.74	*0.04*	0.12	*0.02*	0.41	*0.02*	55.85	*0.25*	BDL	-	0.06	*0.01*	41.04	*0.39*	98.73			
F163	g	19	49.5 (-0.9/+3.1)	60.44	*0.61*	0.44	*0.03*	19.18	*0.36*	6.29	*0.19*	0.17	*0.01*	3.04	*0.29*	6.64	*0.19*	1.5	*0.11*	1.55	*0.22*	0.75	*0.04*	87.35	0.46		
	ol	13	2.6 (-1.7/+1.1)	38.82	*0.38*	0.02	*0.02*	0.02	*0.01*	21.25	*0.93*	0.4	*0.02*	39.7	*0.9*	0.16	*0.06*	BDL	-	BDL	-	0.26	*0.22*	100.65	0.77	0.26	
	cpx	12	9.0 (-1.8/+1.8)	53.27	*0.48*	0.44	*0.09*	2.47	*0.99*	6.79	*0.59*	0.23	*0.03*	15.79	*0.72*	20.58	*0.96*	0.49	*0.26*	0.04	*0.03*	0.05	*0.05*	100.16	0.81	0.21	
	opx	12	2.8 (-1.8/+1.1)	54.06	*0.59*	0.13	*0.02*	2.4	*0.57*	15.78	*0.26*	0.52	*0.02*	26.19	*0.29*	1.44	*0.3*	0.02	*0.01*	BDL	-	BDL	-	100.57	0.75	0.29	
	amph	16	36.3 (-3.7/+4.7)	44.9	*0.61*	1.41	*0.21*	11.35	*0.64*	9.49	*0.25*	0.18	*0.02*	16.38	*0.27*	10.94	*0.24*	2.12	*0.05*	0.76	*0.08*	0.03	*0.01*	97.57	0.75	0.28	3.2
OD173	g	19	70.1 (-1.6/+1.8)	56.91	*0.35*	0.99	*0.03*	18.87	*0.17*	6.91	*0.18*	0.16	*0.01*	4.19	*0.19*	7.79	*0.21*	1.79	*0.15*	1.91	*0.25*	0.49	*0.03*	88.44	0.52		
	ol	13	9.8 (-0.8/+0.7)	39.14	*0.32*	0.04	*0.02*	BDL	-	19.01	*0.99*	0.34	*0.02*	41.3	*0.89*	0.24	*0.08*	BDL	-	BDL	-	0.39	*0.11*	100.48	0.79	0.28	
	cpx	17	20.1 (-1.9/+1.8)	53.28	*0.64*	0.65	*0.44*	1.6	*1.01*	5.92	*0.87*	0.19	*0.05*	16.49	*0.61*	21.61	*0.73*	0.59	*0.49*	0.03	*0.02*	0.06	*0.07*	100.44	0.83	0.22	
F153	g	13	72.7 (-0.9/+0.9)	53.98	*0.39*	0.96	*0.03*	19.27	*0.27*	6.78	*0.19*	0.17	*0.01*	4.99	*0.21*	8.95	*0.18*	2.61	*0.19*	1.83	*0.1*	0.47	*0.02*	88.66	0.57		
	ol	13	11.0 (-0.6/+0.6)	39.35	*0.33*	0.04	*0.02*	0.02	*0.02*	18.13	*1.11*	0.36	*0.02*	42.26	*0.58*	0.2	*0.03*	BDL	-	BDL	-	0.24	*0.21*	100.58	0.81	0.32	
	cpx	8	16.3 (-0.9/+0.8)	53.15	*0.75*	0.3	*0.05*	1.77	*0.26*	5.33	*0.2*	0.19	*0.02*	16.87	*0.48*	22.52	*0.28*	0.17	*0.02*	BDL	-	BDL	-	100.32	0.85	0.23	
F174	g	16	38.9 (-1.5/+2.1)	65.65	*0.85*	0.32	*0.06*	19.67	*0.17*	4.62	*0.43*	0.17	*0.03*	1.61	*0.25*	5.07	*0.19*	1.47	*0.17*	0.89	*0.08*	0.52	*0.11*	87.92	0.38		
	opx	15	2.8 (-1.7/+1.1)	54.39	*0.46*	0.14	*0.02*	2.05	*0.41*	17.38	*0.58*	0.53	*0.02*	24.7	*0.64*	1.4	*0.13*	0.02	*0.01*	0.03	*0.01*	BDL	-	100.66	0.72	0.25	
	amph	17	57.1 (-2.7/+3.2)	46.24	*0.49*	1.16	*0.08*	10.82	*0.42*	10.46	*0.37*	0.22	*0.02*	15.76	*0.66*	10.73	*0.34*	1.8	*0.09*	0.63	*0.1*	0.06	*0.03*	97.89	0.73	0.23	3.6
	ap	5	1.2 (-0.3/+0.3)	1.02	*1.45*	0.02	*0.02*	0.18	*0.16*	0.68	*0.05*	0.1	*0.02*	0.46	*0.12*	54.84	*0.27*	0.02	*0.01*	0.08	*0.03*	41.2	*1.61*	98.58			
F175	g	13	68.0 (-0.8/+0.9)	57.56	*0.28*	1.01	*0.04*	19.52	*0.21*	6.11	*0.22*	0.15	*0.01*	3.44	*0.36*	7.82	*0.13*	2.02	*0.09*	1.85	*0.07*	0.52	*0.03*	89.57	0.5		
	ol	15	12.4 (-0.8/+0.7)	39.31	*0.27*	0.03	*0.02*	0.03	*0.03*	20.63	*0.36*	0.39	*0.02*	39.57	*0.59*	0.3	*0.2*	BDL	-	BDL	-	0.11	*0.1*	100.37	0.77	0.29	
	cpx	10	19.6 (-0.9/+0.9)	53.41	*0.72*	0.61	*0.19*	2	*0.59*	6.21	*0.71*	0.22	*0.05*	16.01	*0.75*	21.7	*0.68*	0.55	*0.35*	0.03	*0.02*	0.04	*0.04*	100.79	0.82	0.22	
OD143	g	9	46.0 (-1.8/+2.1)	57.08	*0.47*	0.91	*0.02*	20.21	*0.2*	6.73	*0.25*	0.16	*0.02*	3.88	*0.48*	7.62	*0.4*	1.31	*0.14*	1.46	*0.38*	0.64	*0.03*	88.49	0.51		
	cpx	7	21.8 (-1.2/+1.4)	52.73	*0.32*	0.5	*0.1*	3.14	*0.7*	6.81	*0.71*	0.26	*0.09*	16.37	*0.44*	20.26	*0.52*	0.54	*0.16*	0.03	*0.02*	0.11	*0.19*	100.75	0.81	0.24	
	opx	9	6.3 (-1.1/+1.0)	53.64	*0.42*	0.22	*0.03*	3.64	*0.4*	13.48	*0.22*	0.34	*0.02*	27.57	*0.43*	1.65	*0.29*	0.03	*0.01*	BDL	-	BDL	-	100.59	0.78	0.28	
	amph	10	26.0 (-1.9/+1.9)	42.79	*0.43*	1.96	*0.08*	13.93	*0.49*	8.45	*0.2*	0.14	*0.01*	16.14	*0.4*	11.07	*0.34*	2.31	*0.06*	1.03	*0.06*	0.04	*0.01*	97.86	0.77	0.30	2.2
F204	g	16	69.5 (-0.4/+1.6)	56.14	*0.3*	1.04	*0.04*	19.45	*0.18*	7.07	*0.12*	0.16	*0.01*	4.44	*0.31*	7.7	*0.19*	1.61	*0.15*	1.87	*0.2*	0.52	*0.04*	88.78	0.53		
	ol	7	9.3 (-1.0/+1.0)	37.51	*0.36*	0.03	*0.01*	0.05	*0.03*	18.41	*0.83*	0.31	*0.03*	42.55	*0.77*	0.17	*0.03*	BDL	-	BDL	-	0.13	*0.11*	99.17	0.8	0.27	
	cpx	9	19.4 (-1.2/+1.4)	52.28	*0.75*	0.61	*0.38*	1.66	*0.73*	5.54	*0.5*	0.19	*0.05*	16.98	*0.6*	21.58	*1.03*	0.62	*0.32*	0.02	*0.01*	0.02	*0.03*	99.51	0.85	0.20	
	opx	10	1.8 (-1.6/+0.8)	53.4	*0.62*	0.18	*0.02*	2.17	*0.53*	11.69	*0.55*	0.33	*0.02*	29.56	*0.41*	1.58	*0.16*	0.02	*0.01*	BDL	-	BDL	-	98.93	0.82	0.25	
OD141	g	15	75.0 (-1.2/+2.6)	57.1	*0.12*	0.96	*0.02*	16.85	*0.08*	6.73	*0.07*	0.17	*0.01*	6.07	*0.09*	8.55	*0.09*	1.37	*0.04*	1.73	*0.1*	0.47	*0.03*	89.35	0.62		
	ol	19	8.5 (-0.7/+0.8)	39.11	*0.31*	0.02	*0.01*	0.02	*0.03*	17.94	*0.89*	0.32	*0.01*	42.01	*0.98*	0.28	*0.43*	BDL	-	BDL	-	0.07	*0.03*	99.76	0.81	0.39	
	cpx	9	15.3 (-1.6/+1.7)	53.55	*0.54*	0.32	*0.07*	2.11	*0.24*	5.76	*0.43*	0.21	*0.02*	17.59	*0.35*	20.55	*0.52*	0.28	*0.09*	BDL	-	0.02	*0.02*	100.38	0.84	0.30	
	opx	23	1.3 (-1.4/+0.7)	54.99	*0.53*	0.19	*0.02*	2.55	*0.51*	11.17	*0.39*	0.3	*0.02*	29.32	*0.41*	1.68	*0.13*	0.02	*0.01*	BDL	-	BDL	-	100.23	0.82	0.34	
OD155	g	17	63.8 (-1.2/+1.4)	54.89	*0.31*	1.14	*0.07*	19.63	*0.17*	6.99	*0.16*	0.16	*0.02*	3.83	*0.16*	6.96	*0.17*	3.25	*0.32*	2.38	*0.16*	0.77	*0.06*	91.25	0.49		
	cpx	13	20.9 (-1.5/+1.5)	52.15	*0.46*	0.52	*0.05*	3.91	*0.51*	6.25	*0.5*	0.25	*0.02*	16.84	*0.49*	19.43	*0.57*	0.47	*0.05*	0.05	*0.03*	0.03	*0.03*	99.88	0.83	0.20	
	opx	12	15.4 (-1.2/+1.1)	53.83	*0.46*	0.26	*0.05*	3.43	*0.54*	10.92	*0.94*	0.3	*0.03*	28.54	*0.69*	1.99	*0.29*	0.05	*0.02*	0.02	*0.02*	BDL	-	99.36	0.82	0.21	
OD153	g	14	77.7 (-1.1/+1.5)	55.17	*0.23*	1.05	*0.03*	17.28	*0.16*	6.26	*0.04*	0.17	*0.02*	6.25	*0.05*	8.49	*0.06*	2.83	*0.03*	1.88	*0.03*	0.63	*0.04*	90.64	0.64		
	cpx	14	11.3 (-1.7/+1.5)	53.72	*0.38*	0.32	*0.06*	2.29	*0.35*	5.1	*0.27*	0.22	*0.02*	18.44	*0.51*	19.82	*0.57*	0.3	*0.12*	0.02	*0.01*	BDL	-	100.23	0.87	0.28	
	opx	13	11.0 (-1.1/+1.1)	55.59	*0.43*	0.19	*0.02*	1.84	*0.48*	9.18	*0.36*	0.28	*0.01*	30.87	*0.34*	2.02	*0.14*	0.03	*0.01*	BDL	-	BDL	-	100	0.86	0.30	
OD150	g	14	79.2 (-1.0/+1.5)	54.39	*0.5*	1.01	*0.02*	16.6	*0.15*	7.47	*0.12*	0.17	*0.02*	6.39	*0.14*	8.89	*0.1*	2.64	*0.05*	1.84	*0.06*	0.6	*0.02*	92.13	0.6		
	cpx	7	10.0 (-1.7/+1.4)	52.58	*0.86*	0.26	*0.02*	2.24	*0.24*	5.72	*0.41*	0.2	*0.02*	18.44	*0.28*	19.64	*0.66*	0.28	*0.02*	BDL	-	BDL	-	99.39	0.85	0.27	
	opx	12	10.8 (-1.1/+1.0)	55.9	*0.54*	0.14	*0.02*	1.52	*0.26*	8.5	*0.89*	0.26	*0.02*	31.17	*0.66*	2.3	*0.31*	0.04	*0.01*	BDL	-	BDL	-	99.86	0.87	0.23	
F230	g	19	74.6 (-0.8/+4.8)	57.39	*0.53*	1.03	*0.03*	17.75	*0.16*	5.61	*0.39*	0.15	*0.01*	4.67	*0.17*	7.59	*0.2*	3.09	*0.12*	2.08	*0.09*	0.65	*0.04*	92.78	0.6		
	ol	10	5.2 (-2.7/+1.9)	39.69	*0.57*	0.05	*0.01*	0.03	*0.02*	15.55	*0.51*	0.33	*0.03*	44.32	*0.87*	0.21	*0.02*	BDL	-	BDL	-	0.17	*0.14*	100.35	0.84	0.29	
	cpx	16	13.2 (-2.2/+2.6)	53.35	*0.77*	0.52	*0.1*	2.27	*0.48*	5.32	*0.79*	0.27	*0.08*	17.47	*0.88*	20.75	*1.25*	0.3	*0.09*	0.05	*0.02*	0.04	*0.03*	100.35	0.85	0.25	
	opx	9	7.1 (-3.9/+2.7)	55.37	*0.76*	0.29	*0.03*	2.3	*0.35*	9.07	*0.32*	0.33	*0.02*	30.37	*0.8*	2.01	*0.23*	0.03	*0.01*	0.05	*0.04*	0.02	*0.02*	99.83	0.86	0.25	
F137	g	12	41.8 (-2.0/+2.0)	56.23	*0.66*	0.76	*0.03*	22.27	*0.37*	4.64	*0.15*	0.12	*0.01*	4.59	*0.35*	8.12	*0.17*	2.14	*0.15*	0.85	*0.1*	0.28	*0.04*	88.5	0.64		
	ol	15	21.9 (-0.7/+0.8)	39.82	*0.43*	0.03	*0.02*	0.03	*0.01*	15.53	*0.44*	0.27	*0.02*	44.26	*0.64*	0.13	*0.03*	BDL	-	BDL	-	0.3	*0.17*	100.38	0.84	0.35	
	amph	14	36.3 (-2.4/+2.4)	45.21	*0.8*	1.34	*0.12*	12.49	*0.84*	6.2	*0.15*	0.11	*0.02*	17.72	*0.33*	11.43	*0.1*	2.38	*0.08*	0.33	*0.01*	0.02	*0.02*	97.23	0.84	0.35	1.8
F145	g	17	61.1 (-2.1/+2.3)	57.43	*0.25*	0.85	*0.05*	19.02	*0.12*	5.56	*0.16*	0.14	*0.03*	4.96	*0.18*	8.47	*0.18*	2.33	*0.11*	1.01	*0.06*	0.25	*0.02*	88.42	0.61		
	ol	22	26.0 (-0.7/+0.9)	40.14	*0.34*	0.03	*0.02*	0.02	*0.02*	13.01	*1.5*	0.26	*0.04*	46.53	*1.23*	0.14	*0.02*	BDL	-	BDL	-	0.2	*0.13*	100.34	0.86	0.25	
	cpx	21	13.0 (-2.2/+1.9)	53.26	*0.77*	0.29	*0.07*	2.11	*0.5*	4.85	*0.45*	0.17	*0.04*	17.47	*0.31*	21.79	*0.57*	0.21	*0.04*	BDL	-	BDL	-	100.17	0.87	0.25	
F125	g	10	75.7 (-0.8/+0.9)	56.72	*0.26*	0.81	*0.03*	17.96	*0.24*	6.14	*0.11*	0.14	*0.02*	6.69	*0.31*	8.08	*0.27*	2.34	*0.32*	0.85	*0.03*	0.26	*0.04*	87.9	0.66		
	ol	16	24.3 (-0.9/+0.8)	40.6	*0.88*	0.02	*0.02*	0.03	*0.03*	11.36	*0.67*	0.2	*0.01*	48.25	*0.95*	0.12	*0.02*	BDL	-	BDL	-	0.12	*0.13*	100.7	0.88	0.26	
OD168	g	10	51.1 (-1.5/+2.3)	61.81	*0.48*	0.51	*0.05*	20.1	*0.25*	5.44	*0.32*	0.16	*0.02*	2.55	*0.37*	6.04	*0.23*	2.11	*0.36*	0.9	*0.14*	0.39	*0.06*	87.8	0.45		
	opx	8	2.2 (-1.5/+0.9)	54.08	*1.04*	0.15	*0.03*	2.39	*0.87*	15.04	*0.61*	0.45	*0.02*	26.72	*1.02*	1.25	*0.1*	BDL	-	BDL	-	BDL	-	100.1	0.76	0.26	
	amph	8	46.6 (-2.3/+2.7)	45.64	*0.61*	1.06	*0.08*	12.21	*0.54*	9.92	*0.76*	0.21	*0.01*	16.22	*0.52*	10.49	*0.33*	2.17	*0.05*	0.27	*0.02*	0.05	*0.02*	98.23	0.74	0.29	2.1
OD109	g	15	59.2 (-1.3/+2.1)	59.58	*0.27*	0.56	*0.05*	19.71	*0.15*	6.2	*0.15*	0.19	*0.03*	3.55	*0.08*	7.13	*0.18*	1.85	*0.31*	0.89	*0.12*	0.34	*0.02*	87.78	0.51		
	opx	11	3.0 (-1.5/+1.0)	54.77	*0.65*	0.15	*0.05*	2.47	*0.72*	12.71	*0.73*	0.4	*0.04*	28.56	*0.76*	1.36	*0.14*	0.02	*0.01*	BDL	-	BDL	-	100.44	0.8	0.25	
	amph	34	37.8 (-2.4/+2.6)	45.48	*0.73*	1.12	*0.08*	11.63	*0.5*	8.57	*0.36*	0.18	*0.04*	17.09	*0.42*	10.94	*0.38*	2.27	*0.06*	0.29	*0.03*	0.02	*0.03*	97.58	0.78	0.29	2.0
OD166	g	16	77.3 (-1.0/+1.2)	57.17	*0.23*	0.87	*0.02*	19.74	*0.06*	6.14	*0.14*	0.16	*0.01*	4.33	*0.12*	7.94	*0.12*	2.12	*0.12*	1.26	*0.1*	0.27	*0.03*	88.75	0.56		
	ol	7	8.9 (-0.7/+0.7)	39.2	*0.23*	0.02	*0.01*	BDL	-	19.36	*0.7*	0.37	*0.01*	41.48	*0.56*	0.12	*0.03*	BDL	-	BDL	-	0.08	*0.09*	100.62	0.79	0.33	
	cpx	7	13.9 (-1.3/+1.2)	53.26	*1.25*	0.59	*0.17*	2.06	*0.9*	6.37	*0.29*	0.2	*0.04*	16.46	*1.07*	20.68	*0.97*	0.99	*0.56*	BDL	-	0.05	*0.02*	100.67	0.82	0.27	
OD160	g	15	76.7 (-1.1/+1.2)	58.06	*0.1*	0.78	*0.03*	20.05	*0.11*	5.77	*0.11*	0.16	*0.01*	4.08	*0.11*	7.75	*0.1*	2.1	*0.09*	1	*0.04*	0.26	*0.03*	88.59	0.56		
	ol	11	8.9 (-0.6/+0.6)	39.65	*0.74*	0.04	*0.02*	0.07	*0.1*	16.53	*1.02*	0.34	*0.02*	42.68	*1.19*	0.44	*0.39*	BDL	-	BDL	-	0.24	*0.17*	100	0.82	0.27	
	cpx	11	14.4 (-1.4/+1.3)	53.6	*0.68*	0.33	*0.04*	2.44	*0.78*	6.04	*0.56*	0.22	*0.03*	16.52	*0.51*	20.88	*0.54*	0.46	*0.41*	BDL	-	BDL	-	100.53	0.83	0.26	
OD161	g	15	82.7 (-0.9/+1.2)	57.24	*0.25*	0.75	*0.03*	19.23	*0.18*	5.63	*0.13*	0.18	*0.02*	4.92	*0.18*	8.41	*0.35*	2.66	*0.18*	0.74	*0.12*	0.26	*0.02*	87.88	0.61		
	ol	14	9.6 (-0.7/+0.7)	39.61	*0.24*	BDL	-	BDL	-	17.02	*0.36*	0.35	*0.01*	42.62	*0.33*	0.13	*0.04*	BDL	-	BDL	-	0.07	*0.08*	99.81	0.82	0.35	

	cpx	14	7.8 (-1.3/+1.1)	53.9	*0.46*	0.31	*0.18*	1.96	*0.38*	4.98	*0.31*	0.21	*0.03*	17.08	*0.38*	21.49	*0.53*	0.29	*0.18*	BDL	-	0.02	*0.04*	100.25	0.86	0.25	
OD167	g	17	90.3 (-0.7/+0.7)	55.97	*0.24*	0.82	*0.03*	18.65	*0.17*	6.33	*0.15*	0.17	*0.02*	5.57	*0.22*	8.66	*0.25*	2.94	*0.4*	0.66	*0.04*	0.23	*0.02*	89.09	0.61		
	ol	6	9.7 (-0.7/+0.7)	38.85	*0.58*	0.06	*0.02*	0.02	*0.01*	16.01	*0.55*	0.32	*0.02*	44.69	*0.66*	0.19	*0.04*	BDL	-	BDL	-	0.3	*0.17*	100.44	0.83	0.32	
OD163	g	14	91.4 (-0.6/+0.7)	55.62	*0.5*	0.81	*0.03*	17.66	*0.13*	6.43	*0.15*	0.17	*0.01*	6.01	*0.23*	8.74	*0.18*	3.53	*0.34*	0.81	*0.07*	0.23	*0.02*	87.82	0.62		
	ol	4	8.6 (-0.7/+0.6)	37.4	*0.21*	0.02	*0.01*	0.03	*0.02*	14.56	*0.43*	0.3	*0.01*	46.74	*1*	0.13	*0.01*	BDL	-	BDL	-	0.03	*0.01*	99.21	0.85	0.29	
OD144	g	13	40.3 (-2.2/+3.5)	58.56	*0.7*	0.77	*0.03*	20.67	*0.41*	5.74	*0.45*	0.17	*0.03*	3.44	*1*	8.53	*0.72*	1.03	*0.27*	0.77	*0.3*	0.32	*0.02*	86.66	0.51		
	cpx	7	1.2 (-1.2/+0.6)	52.48	*0.53*	0.49	*0.09*	3.51	*0.62*	6.41	*0.61*	0.22	*0.01*	16.28	*0.44*	20.86	*0.28*	0.47	*0.12*	BDL	-	0.02	*0.02*	100.74	0.82	0.24	
	opx	9	1.7 (-1.4/+0.8)	53.16	*0.79*	0.22	*0.02*	4.79	*0.88*	11.97	*0.73*	0.32	*0.01*	28.4	*0.55*	1.69	*0.22*	0.05	*0.01*	BDL	-	BDL	-	100.61	0.81	0.25	
	amph	9	56.9 (-2.5/+4.3)	44.01	*0.4*	1.59	*0.22*	13.62	*0.44*	8.25	*0.21*	0.16	*0.01*	16.95	*0.36*	10.76	*0.22*	2.57	*0.08*	0.32	*0.02*	0.02	*0.01*	98.25	0.79	0.29	2.1
OD142	g	15	74.6 (-0.9/+1.1)	56.65	*0.26*	0.89	*0.02*	20.42	*0.36*	6.06	*0.14*	0.16	*0.02*	4.7	*0.15*	8.32	*0.12*	1.84	*0.11*	0.67	*0.08*	0.29	*0.02*	88.86	0.58		
	cpx	14	14.4 (-1.2/+1.2)	53.35	*0.42*	0.33	*0.06*	2.77	*0.43*	5.65	*0.26*	0.22	*0.02*	17.47	*0.6*	20.29	*0.69*	0.33	*0.07*	BDL	-	BDL	-	100.42	0.85	0.25	
	opx	21	11.1 (-0.9/+0.8)	54.93	*0.65*	0.18	*0.02*	3.16	*0.57*	9.89	*0.63*	0.31	*0.02*	29.94	*0.52*	1.73	*0.25*	0.03	*0.01*	BDL	*0.01*	BDL	-	100.17	0.84	0.26	
OD169	g	19	45.9 (-1.8/+4.2)	61.25	*0.96*	1.12	*0.06*	19.6	*0.65*	4.77	*0.2*	0.1	*0.02*	1.8	*0.08*	4.98	*0.19*	3.7	*0.38*	2.11	*0.12*	0.56	*0.05*	88.25	0.4		
	cpx	13	12.3 (-2.1/+2.4)	51.91	*1.08*	0.86	*0.08*	5.67	*1.09*	8.12	*0.84*	0.23	*0.04*	14.75	*0.79*	17.95	*1.1*	0.66	*0.15*	0.06	*0.02*	0.04	*0.02*	100.25	0.76	0.21	
	opx	15	10.9 (-2.4/+2.4)	52.62	*0.92*	0.35	*0.05*	4.46	*0.58*	14.78	*1.19*	0.31	*0.03*	25.06	*1.04*	2.08	*0.63*	0.11	*0.04*	0.03	*0.02*	0.02	*0.02*	99.81	0.75	0.22	
	amph	15	21.9 (-5.0/+4.9)	42.25	*1.06*	3.7	*0.35*	12.86	*0.81*	11.33	*0.38*	0.18	*0.02*	14.15	*1.03*	9.82	*0.69*	2.63	*0.24*	0.46	*0.04*	0.06	*0.02*	97.45	0.69	0.30	3.3
	plag	11	9.1 (-2.9/+2.6)	53.83	*0.9*	0.07	*0.05*	29.57	*0.61*	0.42	*0.18*	BDL	-	0.1	*0.07*	11.18	*0.52*	5.03	*0.26*	0.21	*0.04*	BDL	*0.03*	100.41			
OD171	g	16	69.2 (-1.3/+2.2)	58.34	*0.19*	0.96	*0.03*	20.09	*0.12*	5.27	*0.08*	0.12	*0.01*	2.95	*0.04*	6.44	*0.08*	4.05	*0.07*	1.4	*0.02*	0.38	*0.02*	92.98	0.5		
	cpx	9	12.7 (-0.8/+1.0)	52.14	*0.55*	0.71	*0.08*	5.35	*0.87*	7.29	*0.36*	0.23	*0.06*	15.38	*1.27*	18.8	*0.73*	0.6	*0.11*	0.04	*0.02*	0.03	*0.03*	100.57	0.79	0.27	
	opx	10	15.9 (-0.7/+1.0)	53.5	*0.53*	0.31	*0.04*	4.69	*0.53*	13.41	*0.34*	0.28	*0.03*	25.86	*0.56*	1.86	*0.24*	0.07	*0.02*	0.03	*0.02*	0.02	*0.03*	100.03	0.77	0.29	
	plag	11	2.2 (-1.9/+1.0)	52.83	*0.46*	0.05	*0.02*	29.61	*0.79*	0.38	*0.18*	BDL	-	0.2	*0.44*	12.28	*0.42*	4.53	*0.21*	0.15	*0.01*	BDL	-	100.04			
OD170	g	15	75.0 (-0.8/+1.1)	57.92	*0.51*	0.88	*0.05*	20.07	*0.24*	5.92	*0.17*	0.12	*0.02*	3.04	*0.16*	6.91	*0.21*	3.59	*0.14*	1.19	*0.07*	0.36	*0.05*	92.05	0.48		
	cpx	14	10.2 (-1.3/+1.1)	51.94	*0.78*	0.54	*0.06*	4.33	*1.03*	8.43	*0.54*	0.25	*0.07*	15.95	*0.78*	18.24	*0.86*	0.58	*0.11*	0.02	*0.01*	0.02	*0.02*	100.31	0.77	0.27	
	opx	13	14.8 (-0.8/+0.8)	53.13	*0.9*	0.27	*0.03*	4.3	*0.66*	13.85	*1.06*	0.3	*0.03*	26	*0.99*	2.02	*0.37*	0.06	*0.02*	BDL	-	BDL	-	99.97	0.77	0.27	
OD172	g	15	75.5 (-1.2/+1.4)	57.76	*0.36*	0.9	*0.04*	19.21	*0.25*	5.72	*0.13*	0.13	*0.02*	3.83	*0.25*	7.65	*0.14*	3.4	*0.23*	1.08	*0.03*	0.32	*0.05*	92.74	0.54		
	cpx	11	8.6 (-1.5/+1.3)	51.93	*0.67*	0.51	*0.1*	4.96	*1.17*	6.95	*0.43*	0.25	*0.03*	16.35	*0.72*	18.4	*0.8*	0.55	*0.07*	0.03	*0.02*	0.03	*0.02*	99.97	0.81	0.28	
	opx	10	15.9 (-0.8/+0.8)	53.83	*0.76*	0.25	*0.05*	4.03	*0.76*	11.57	*0.64*	0.28	*0.03*	28.03	*1.03*	2.13	*0.41*	0.07	*0.03*	BDL	-	BDL	-	100.22	0.81	0.28	
F233	g	20	88.9 (-0.8/+0.8)	56.79	*0.19*	0.81	*0.03*	18.21	*0.2*	6.42	*0.13*	0.16	*0.02*	4.94	*0.32*	9.17	*0.16*	2.59	*0.07*	0.69	*0.03*	0.22	*0.02*	89.9	0.58		
	ol	14	11.1 (-0.8/+0.8)	39.25	*0.47*	0.03	*0.01*	BDL	-	16.97	*1.04*	0.35	*0.03*	43.14	*0.85*	0.21	*0.05*	BDL	-	BDL	-	0.27	*0.19*	100.25	0.82	0.30	
F228	g	16	90.6 (-1.0/+1.2)	56.95	*0.16*	0.85	*0.02*	18.74	*0.29*	6.32	*0.14*	0.17	*0.02*	5.29	*0.18*	8.53	*0.11*	2.21	*0.05*	0.72	*0.04*	0.23	*0.02*	90.15	0.6		
	ol	5	9.3 (-1.2/+1.0)	39.69	*0.57*	0.02	*0.02*	0.05	*0.05*	16.07	*0.66*	0.35	*0.02*	44.14	*0.84*	0.19	*0.02*	BDL	-	BDL	-	0.15	*0.23*	100.67	0.83	0.30	
F236	g	19	55.4 (-2.1/+2.4)	56.55	*0.39*	1.02	*0.04*	16.71	*0.11*	8.39	*0.16*	0.16	*0.01*	4.1	*0.1*	7.06	*0.13*	4.23	*0.11*	1.47	*0.03*	0.32	*0.03*	96.5	0.47		
	cpx	9	9.6 (-1.3/+1.2)	50.31	*0.82*	0.48	*0.07*	4.61	*0.68*	8.47	*0.73*	0.24	*0.03*	16.11	*0.78*	18.63	*0.66*	0.52	*0.05*	0.02	*0.01*	BDL	-	99.38	0.77	0.26	
	opx	9	17.0 (-0.9/+1.0)	54.89	*0.63*	0.22	*0.04*	2.49	*0.59*	10.52	*0.87*	0.27	*0.01*	29	*1.14*	2.47	*0.26*	0.05	*0.02*	BDL	-	BDL	-	99.92	0.83	0.18	
	plag	11	18.0 (-1.7/+1.7)	53.2	*0.53*	0.07	*0.05*	29.17	*0.77*	1.12	*0.34*	BDL	-	0.2	*0.14*	11.95	*0.31*	4.56	*0.11*	0.22	*0.04*	BDL	-	100.51			
F231	g	20	92.4 (-0.6/+0.7)	54.51	*0.14*	0.78	*0.03*	16.23	*0.08*	8.52	*0.07*	0.16	*0.01*	6.68	*0.12*	8.38	*0.07*	3.54	*0.04*	0.94	*0.02*	0.25	*0.03*	97.04	0.58		
	opx	12	7.6 (-0.7/+0.6)	55.52	*1.01*	0.14	*0.02*	2	*0.35*	9.04	*0.41*	0.24	*0.02*	31.55	*0.85*	1.88	*0.18*	0.03	*0.01*	BDL	-	BDL	-	100.42	0.86	0.22	
F246	g	15	79.0 (-1.4/+1.4)	60.27	*0.12*	0.51	*0.03*	21.3	*0.05*	4.41	*0.1*	0.2	*0.02*	2.29	*0.09*	7.37	*0.06*	2.28	*0.05*	1.01	*0.03*	0.36	*0.03*	89.02	0.48		
	amph	25	21.0 (-1.4/+1.4)	42.9	*0.65*	1.53	*0.17*	14.44	*0.62*	9.7	*0.31*	0.25	*0.02*	14.59	*0.39*	11.64	*0.19*	2.36	*0.06*	0.41	*0.03*	0.05	*0.07*	97.87	0.73	0.35	3.0
F243	g	15	81.4 (-1.3/+1.4)	59.81	*0.13*	0.56	*0.03*	21.07	*0.06*	4.68	*0.12*	0.21	*0.02*	2.56	*0.11*	7.59	*0.05*	2.19	*0.07*	0.98	*0.03*	0.36	*0.03*	89.05	0.49		
	amph	28	18.6 (-1.4/+1.3)	44.02	*1.63*	1.48	*0.2*	13.4	*1.88*	8.79	*0.89*	0.23	*0.04*	15.51	*0.28*	12.04	*1.39*	2.4	*0.07*	0.4	*0.06*	0.04	*0.03*	98.3	0.76	0.31	2.6
F237	g	15	95.8 (-0.8/+2.1)	56.76	*0.29*	0.75	*0.04*	19.98	*0.09*	5.45	*0.06*	0.2	*0.02*	4.43	*0.08*	8.47	*0.1*	2.69	*0.06*	1	*0.04*	0.28	*0.03*	88.71	0.59		
	ol	7	1.3 (-0.6/+0.4)	39.71	*0.51*	0.03	*0.01*	0.03	*0.04*	15.99	*0.48*	0.46	*0.02*	43.4	*0.58*	0.35	*0.41*	BDL	-	BDL	-	0.14	*0.12*	100.13	0.83	0.30	
	cpx	6	2.9 (-1.8/+1.1)	53.68	*0.75*	0.95	*0.23*	0.84	*0.25*	5.92	*0.7*	0.24	*0.08*	14.84	*0.52*	21.6	*0.57*	2.1	*0.38*	0.02	*0.01*	0.07	*0.04*	100.27	0.82	0.32	
OD176	g	21	64.9 (-2.2/+3.3)	64.62	*0.41*	0.34	*0.03*	21.5	*0.16*	2.73	*0.24*	0.17	*0.03*	0.94	*0.14*	6.53	*0.12*	1.85	*0.12*	1.06	*0.04*	0.26	*0.03*	86.77	0.38		
	amph	11	32.1 (-1.5/+2.3)	41.23	*1.08*	1.43	*0.13*	15.98	*1.64*	11.74	*0.43*	0.31	*0.02*	12.79	*0.65*	11.5	*0.41*	2.37	*0.13*	0.47	*0.06*	0.15	*0.37*	97.97	0.66	0.32	4.2
	plag	8	3.0 (-2.3/+1.3)	45.36	*0.51*	BDL	-	35.35	*0.54*	0.37	*0.04*	BDL	-	0.02	*0.01*	17.81	*0.25*	1.47	*0.13*	0.03	*0.01*	0.04	*0.06*	100.47			
OD179	g	20	66.3 (-1.7/+1.8)	63.21	*0.34*	0.43	*0.04*	21.75	*0.21*	3.09	*0.28*	0.18	*0.03*	1.13	*0.23*	6.91	*0.1*	1.94	*0.17*	1.06	*0.05*	0.31	*0.05*	86.59	0.39		
	amph	17	33.7 (-1.8/+1.7)	42.05	*0.89*	1.41	*0.22*	15.43	*0.96*	11.54	*1.42*	0.3	*0.02*	13.12	*0.79*	11.19	*0.45*	2.37	*0.1*	0.47	*0.04*	0.12	*0.24*	97.98	0.67	0.32	3.3
OD175	g	19	75.5 (-1.5/+1.5)	60.66	*0.35*	0.53	*0.03*	21.3	*0.2*	4.32	*0.09*	0.19	*0.01*	1.93	*0.03*	7.44	*0.16*	2.09	*0.1*	1.17	*0.03*	0.37	*0.03*	84.97	0.44		
	amph	17	24.5 (-1.5/+1.5)	40.77	*0.7*	1.32	*0.13*	14.65	*0.76*	10.57	*0.69*	0.26	*0.04*	13.84	*0.59*	11.49	*0.32*	2.45	*0.09*	0.5	*0.04*	0.03	*0.03*	95.87	0.7	0.34	2.5
OD174	g	18	86.9 (-0.8/+2.6)	59	*0.17*	0.63	*0.03*	20.54	*0.05*	5.2	*0.09*	0.2	*0.02*	2.86	*0.05*	7.7	*0.08*	2.29	*0.05*	1.26	*0.05*	0.32	*0.02*	87.87	0.49		
	cpx	6	2.3 (-1.8/+1.0)	52.88	*0.62*	1.03	*0.31*	1.44	*0.35*	5.43	*1.32*	0.2	*0.05*	14.66	*0.61*	22.33	*0.74*	1.58	*0.27*	0.02	*0.01*	0.11	*0.06*	99.68	0.83	0.20	
	amph	15	10.8 (-1.9/+1.8)	43.6	*0.63*	1.4	*0.14*	13.26	*0.54*	8.02	*0.42*	0.21	*0.03*	16.22	*0.46*	11.59	*0.16*	2.51	*0.04*	0.48	*0.02*	BDL	-	97.3	0.78	0.27	2.2
OD177	g	15	33.0 (-7.4/+7.9)	62.23	*0.61*	0.86	*0.08*	19.49	*0.58*	4.67	*0.34*	0.18	*0.02*	1.71	*0.14*	5.08	*0.33*	3.69	*0.35*	1.58	*0.09*	0.51	*0.04*	92.24	0.4		
	cpx	10	7.9 (-2.2/+2.2)	52.58	*1.02*	0.62	*0.22*	4.09	*1.41*	7.94	*2.15*	0.42	*0.16*	14.28	*1.4*	19.41	*2.5*	0.74	*0.3*	0.04	*0.01*	0.13	*0.18*	100.25	0.76	0.20	
	opx	16	9.3 (-2.0/+2.3)	52.1	*0.9*	0.32	*0.05*	3.83	*0.56*	19.51	*1.96*	0.59	*0.05*	21.74	*1.71*	1.88	*0.46*	0.07	*0.03*	BDL	-	0.03	*0.02*	100.07	0.66	0.33	
	amph	14	4.1 (-1.7/+1.4)	42.74	*0.69*	2.97	*0.4*	14.28	*0.9*	11.72	*1.11*	0.28	*0.02*	13.13	*0.7*	10.04	*0.46*	2.69	*0.12*	0.39	*0.05*	0.04	*0.01*	98.28	0.67	0.33	3.5
	plag	9	45.8 (-5.7/+7.6)	54.27	*1.28*	0.1	*0.1*	28.87	*1.51*	0.59	*0.52*	0.04	*0.01*	0.18	*0.19*	10.43	*0.8*	5.14	*0.27*	0.23	*0.09*	0.07	*0.07*	99.91			
OD178	g	20	94.1 (-0.4/+1.5)	58.61	*0.25*	0.76	*0.03*	20.09	*0.1*	4.85	*0.11*	0.19	*0.02*	3.24	*0.06*	6.78	*0.12*	3.89	*0.06*	1.22	*0.03*	0.36	*0.03*	94.53	0.54		
	cpx	9	3.7 (-1.5/+1.1)	52.42	*0.55*	0.61	*0.07*	4.92	*0.73*	6.86	*0.77*	0.37	*0.04*	15.15	*0.49*	19.78	*0.54*	0.59	*0.1*	0.03	*0.01*	0.03	*0.01*	100.75	0.8	0.30	
	opx	14	2.2 (-0.8/+0.6)	53.19	*0.86*	0.29	*0.06*	5.03	*0.94*	13.88	*0.92*	0.5	*0.03*	25.91	*1.19*	1.84	*0.21*	0.05	*0.01*	BDL	-	BDL	-	100.72	0.77	0.36	
F245	g	19	55.1 (-3.6/+4.4)	66.96	*0.39*	0.73	*0.04*	17.66	*0.12*	3.95	*0.23*	0.13	*0.02*	1.13	*0.04*	3.74	*0.22*	3.49	*0.16*	1.86	*0.06*	0.34	*0.16*	92.66	0.34		
	cpx	8	18.9 (-1.7/+2.0)	54.33	*0.54*	0.48	*0.18*	2.79	*0.89*	7.53	*0.84*	0.29	*0.05*	14.16	*0.74*	20.32	*1.1*	0.71	*0.29*	0.06	*0.02*	0.06	*0.02*	100.74	0.77	0.15	
	opx	12	5.3 (-1.6/+1.3)	52.04	*0.88*	0.34	*0.04*	2.25	*0.29*	22.91	*1.48*	0.74	*0.03*	20.16	*1.29*	1.95	*0.12*	0.04	*0.01*	BDL	-	0.02	*0.01*	100.46	0.61	0.33	
	plag	8	20.7 (-3.8/+3.6)	55.14	*1.87*	0.09	*0.05*	28.59	*1.26*	0.59	*0.21*	0.03	*0.03*	0.1	*0.07*	10.28	*0.93*	5.28	*0.34*	0.21	*0.07*	0.05	*0.03*	100.36			
F242	g	14	62.4 (-2.9/+4.3)	62.68	*0.53*	0.88	*0.03*	18.62	*0.25*	4.91	*0.45*	0.17	*0.02*	1.92	*0.07*	5	*0.15*	3.75	*0.18*	1.62	*0.08*	0.45	*0.04*	94.2	0.41		
	cpx	13	15.7 (-2.1/+2.2)	53.09	*0.74*	0.74	*0.09*	3.14	*0.71*	8.6	*1.3*	0.45	*0.16*	14.12	*1.05*	19.52	*1.05*	0.63	*0.18*	0.06	*0.03*	0.12	*0.19*	100.46	0.75	0.24	
	opx	11	3.7 (-1.5/+1.1)	53.64	*0.69*	0.34	*0.05*	2.29	*0.62*	16.53	*1.17*	0.63	*0.03*	24.62	*1.04*	2.02	*0.26*	0.04	*0.01*	0.02	*0.01*	0.02	*0.01*	100.14	0.73	0.26	
	plag	10	18.2 (-3.4/+3.2)	54.91	*1.56*	0.2	*0.17*	28.09	*1.78*	1.01	*0.94*	0.05	*0.04*	0.34	*0.33*	10.49	*1.23*	4.91	*0.31*	0.24	*0.07*	0.1	*0.09*	100.34			
F241	g	15	100.0	57.66	*0.11*	0.74	*0.02*	19.25	*0.1*	4.48	*0.09*	0.2	*0.01*	4.38	*0.05*	8.06	*0.07*	3.82	*0.04*	1.08	*0.02*	0.32	*0.02*	95.5	0.64		

Table 4. Details of experiments with equilibrium amphibole + olivine from the compilation of Weber and Blundy (2024).

Study	Experiment IDs	T (°C)	P (GPa)	fO2	H2O	Mineral assemblage	Starting Composition
Barclay and Carmichael (2004)	Jor46.10, Jor46.31, Jor46.21	967-1035	0.104-.0221	NNO+1.3-NNO+2	Saturated	ol+cpx+amph+bt+sp+ap	ne-normative trachybasalt (Cerro la Pilita, TMVB)
Moore and Carmichael (1998)	PEM22-20, PEM22-19	1000	0.250-0.303	~NNO+1-NNO+2	Saturated	ol+amph+/-aug	basaltic andesite (Mascota, TMVB)
Prouteau and Scaillet (2003)	AS12, AS28, AS10, AS11, AS26, AS2	950-1000	0.92		11.4-13.4%	ol+opx+amph+/-cpx+/-phlog	58-59% Pinatubo dacite+41-42% ultramafic grain separates
Andujar et al. (2017)	T6	950	0.2	NNO+1	6.05 wt% (in glass)	ol+cpx+mt+amph	andesite (Tungurahua, Ecuador, Andean NVZ)
Krawczynski et al. (2012)	B1133, B1160, 44-102	1000	0.5-0.8	NNO-NNO+3	Saturated	ol+cpx+amph+/-opx+/-mt	magnesian andesite (85-41c) and basaltic andesite (85-44) (Mt. Shasta, Cascades)
Melekhova et al. (2015)	BM34, BM24	1030-1100	0.7-1	NNO+1.8-5.05	7.2-9.3 wt% (in glass)	ol+cpx+amph+sp+/-quench crystals	basalt (St. Vincent, Lesser Antilles)
Ulmer et al. (2018)	P1060, PU905, PU1005	1000-1060	1	CCOH-NNO+5.5	6.7-9 wt% (in glass)	ol+cpx+opx+amph+sp	high mg# basalt (southern Adamello batholith)